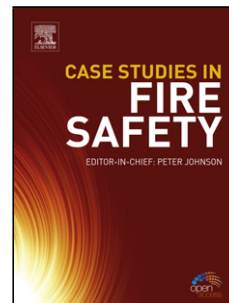


Journal Pre-proof

In situ surface film evolution during Mg aqueous corrosion in presence of selected carboxylates

A. Maltseva (Data curation) (Formal analysis) (Investigation) (Methodology) (Validation) (Visualization) (Writing - original draft) (Writing - review and editing), S.V. Lamaka (Resources) (Supervision) (Validation) (Visualization) (Writing - review and editing), K.A. Yasakau (Investigation) (Validation) (Visualization) (Writing - review and editing), Di Mei (Investigation) (Validation) (Visualization), D. Kurchavov (Investigation) (Validation) (Visualization) (Writing - original draft), M.L. Zheludkevich (Project administration) (Resources) (Writing - review and editing), G. Lefèvre (Investigation) (Methodology) (Supervision) (Formal analysis) (Writing - review and editing), P. Volovitch (Conceptualization) (Methodology) (Visualization) (Project administration) (Funding acquisition) (Supervision) (Writing - original draft) (Writing - review and editing)



PII: S0010-938X(19)31950-X
DOI: <https://doi.org/10.1016/j.corsci.2020.108484>
Reference: CS 108484

To appear in: *Corrosion Science*

Received Date: 16 October 2019
Revised Date: 15 January 2020
Accepted Date: 18 January 2020

Please cite this article as: Maltseva A, Lamaka SV, Yasakau KA, Mei D, Kurchavov D, Zheludkevich ML, Lefèvre G, Volovitch P, *In situ* surface film evolution during Mg aqueous corrosion in presence of selected carboxylates, *Corrosion Science* (2020), doi: <https://doi.org/10.1016/j.corsci.2020.108484>

This is a PDF file of an article that has undergone enhancements after acceptance, such as the addition of a cover page and metadata, and formatting for readability, but it is not yet the definitive version of record. This version will undergo additional copyediting, typesetting and review before it is published in its final form, but we are providing this version to give early visibility of the article. Please note that, during the production process, errors may be discovered which could affect the content, and all legal disclaimers that apply to the journal pertain.

© 2020 Published by Elsevier.

***In situ* surface film evolution during Mg aqueous corrosion in presence of selected carboxylates**

A. Maltseva^{1,*}, S.V. Lamaka², K.A. Yasakau³, Di Mei², D. Kurchavov¹, M.L. Zheludkevich², G. Lefèvre¹, P. Volovitch^{1,*}

¹Chimie ParisTech, PSL Research University, CNRS, Institut de Recherche de Chimie Paris, (IRCP) F-75005 Paris, France

²Magnesium Innovations Centre (MagIC), Helmholtz-Zentrum Geesthacht, Germany

³ Department of Materials and Ceramic Engineering, CICECO - Aveiro institute of materials, University of Aveiro, 3810-193 Aveiro, Portugal

* corresponding authors: alina.maltseva@chimieparistech.psl.eu; polina.volovitch@chimieparistech.psl.eu

Highlights:

- Carboxylates modify kinetics of $\text{Mg}(\text{OH})_2$ film growth on Mg during aqueous corrosion;
- $\text{Mg}(\text{OH})_2$ nano-crystals formed in inhibitors solutions limit Cl^- access to Mg surface;
- Salicylate adsorbs chemically on $\text{Mg}(\text{OH})_2$, dissolves Fe-containing inclusions;
- 2,5-pyridinedicarboxylate precipitates in the form of coordination polymer;
- Inhibition by fumarate seems to be due to adsorption via carboxylate group.

Abstract:

Mechanisms of inhibition of Mg aqueous corrosion in presence of chloride by sodium salicylate (Sal), 2,5-pyridinedicarboxylate (PDC) and fumarate (Fum) were studied by *in situ* Raman spectroscopy, ATR-FTIR, GD-OES and hydrogen collection. *In situ* detected surface films were composed by $\text{Mg}(\text{OH})_2$ nano-crystals and included inhibitors. All carboxylates significantly modified $\text{Mg}(\text{OH})_2$ growth kinetics as well as prevented chloride incorporation in the film. Vibrational spectra of the surface films demonstrated specific interactions between the carboxylates and the surface: adsorption of Sal and Fum on the oxide/hydroxide, precipitation of coordination polymer by PDC, dissolution of iron inclusions via formation of iron-Sal soluble complexes.

Key words:

A. Mg; B. *in situ* Raman spectroscopy; B. Glow Discharge Optical Emission Spectroscopy; B. ATR-FTIR; C. organic inhibitors; C. surface film.

1. Introduction

Corrosion of Mg and its alloys has been extensively studied in recent decades due to their potential application in numerous areas from engineering materials to bio-implants and batteries [1–10]. Particularly, numerous new inhibitors for Mg corrosion are reported regularly [11–18]. In a recent review [11] Mg inhibitors were classified by the mechanism

of their action (anodic, cathodic or mixed type) and by the type of their interaction with the substrate (adsorption/precipitation type). Cathodic inhibition was reported for inorganic anions - phosphates and chromates [13] - as well as for anions containing IV-VI elements As, Se and Ge [16,17,19]. Reduced corrosion rate of Mg-As alloys and strong inhibition effect of soluble arsenates on corrosion rate of Mg [18] were ascribed to the ability of arsenate to poison the cathodic reaction by inhibiting hydrogen recombination [16]. Similar effect was reported for Ge [17].

Salts of carboxylic acids (carboxylates) are often regarded as efficient green corrosion inhibitors for different metals, including Mg [12,20–28]. In the literature, their inhibition effect is generally attributed to the interaction between negatively charged carboxyl groups and the positively charged sites on the metal surface. However, the inhibitions efficiency of carboxylates significantly varies for different metals and environments [12,20–28] and the exact inhibition mechanisms obviously depends on the chemical structure of carboxylate molecule.

For example, carboxylates with the long alkyl carbon chain are believed to be effective inhibitors due to specific interactions (physical or chemical adsorption [27,29]) with metallic surfaces by polar carboxylic group and formation of so-called self-assembled hydrophobic layer due to the aliphatic tail [20,24,27]. Di-(or poly-) carboxylic acids ($\text{HOOC}(\text{CH}_2)_n\text{COOH}$) sometimes demonstrate better corrosion efficiency as compared to their monocarboxylic analogues [22,30]. Presence of additional carboxylic group in the molecule may change the inhibition mechanism. Formation of well-organized adsorption layers on metals is less probable because of the repulsion of COO^- groups for $^-\text{OOC}(\text{CH}_2)_n\text{COO}^-$ chains. Thus, inhibition efficiency in this case is often attributed to formation of weakly soluble salts (or complexes) with cations of the dissolving metal [30].

Carboxylates containing electron donor / acceptor groups (benzene ring, heteroatoms and/or additional functional groups) tend to form stable complexes with metals. Nature of these complexes may play a dual role in terms of corrosion protection. On the one hand, formation of thermodynamically stable soluble complexes with metals can potentially promote metal dissolution [22,31–33]. On the other hand, formation of so-called “surface complexes”, which is basically a chemical adsorption on metal oxides or hydroxides [34], may provide corrosion protection. Very clear example which illustrates these two particular cases is the steel corrosion in presence of benzoate and salicylate anions (salts of benzoic and 2-hydroxybenzoic acids), which are known to form soluble complexes with Fe. Indeed, they do not slow down the active dissolution of iron in neutral aqueous solutions, or can even accelerate it. However, both act as corrosion inhibitors for the oxidized iron surface, preventing the disruption of the passive state by aggressive species such as Cl^- or SO_4^{2-} [22,35–37]. Indeed, these complexing agents were reported to be chemically adsorbed on metal oxides and hydroxides [38–40]. Adsorption of organic molecules can influence the morphology of the formed corrosion products, limiting crystal growth and favoring nucleation [41]. Therefore, formation of the surface complexes can be accompanied by the

reduction of the crystallite size in corrosion products [39,42] and, as a consequence, the formation of more compact surface films which potentially can ensure better corrosion protection.

Carboxylates containing several electron-donor groups (or/and hetero atoms) were reported to form polymeric complexes with the rare-earth metals [43]. Thus, precipitation of long polymeric chains containing rare earth cations and organic ligands was used to explain the synergistic inhibition mechanism in these cases [44,45]. Apparently, not only rare earth metals can form long polymeric chains, synthesis of coordination polymers with Ca [46], Cu [47], Cd, Mn, Ni [48] was reported. Therefore, this phenomenon also should be taken into account when interpreting inhibition mechanism.

Recently, a concept of metal complexing by carboxylates and a balance between stability of different metal complexes provided a basis for a new Mg corrosion inhibition approach proposed by Lamaka et al. [49]. The main idea was based on the suppression of detrimental effect of noble inclusions (mostly, Fe) which are always present in magnesium based engineering materials and can act as local cathodes. Authors assumed that the initial corrosion process leads to the detachment of iron particles from magnesium substrate, these iron particles dissolve with formation of soluble iron cations, which further can be reduced to metallic iron and re-precipitate on the substrate, creating local cathodes and accelerating corrosion [50]. Prevention of the last step due to the complexation of $\text{Fe}^{2+/3+}$ is the general principle of proposed inhibition approach, which has been further extended by testing of more than 150 chemical compounds [12].

Screening of different carboxylates as potential inhibitors for Mg alloys demonstrated very different types of behavior [12,51], even though all types of carboxylates (aliphatic, aromatic (benzene ring) and heterocyclic) carboxylates can be potentially adsorbed on Mg surface and form complexes with Fe. While 2,5 – pyridine-dicarboxylic acid (PDC) and sodium fumarate (Fum) demonstrated high inhibition efficiency for all tested types of Mg (pure Mg, Al- and rare earth containing Mg alloys), the effect of sodium salicylate (Sal) varied significantly as a function of the alloy [51]. Sal inhibited corrosion of Mg alloys and commercial purity Mg (CP-Mg) containing more than 220 ppm of Fe, but it accelerated corrosion of high purity Mg (HP-Mg) containing 51 ppm of Fe. 2,5-PDC and Fum showed the effects characteristic for mixed-type inhibitors, while 3-methyl-salicylate (which is believed to act the same as Sal [12]) performed more as cathodic inhibitor, complying with the iron re-deposition model.

Investigation of the surface film evolution in presence of inhibiting species may clarify some aspects of inhibiting mechanism. Therefore, this article aims to study corrosion products evolution on pure Mg, namely their growth kinetics, morphology, spatial and elemental depth distribution in presence of selected carboxylates (Sal, PDC, Fum) and verify the hypotheses of specific interaction of inhibiting species with corroding Mg surface as well as Fe-complexation involved in the corrosion inhibition mechanism. Surface analysis techniques such as *in situ* Confocal Raman Microscopy (CRM), *ex situ* Attenuated Total

Reflectance Fourier-Transform Infrared Spectroscopy (ATR-FTIR), Glow Discharge Optical Emission Spectroscopy (GD-OES) are used in this work.

2. Experimental details

2.1. Materials and chemicals

As-cast commercial purity magnesium (CP-Mg342) and high purity magnesium (HP-Mg51) were provided by Helmholtz Centrum Geesthacht. The average elemental composition determined by Spark OES (Spark analyser M9, Spectro Ametek, Germany) is presented in **Table 1**. Prior to the experiments, Mg pieces were ground with 800, 1200, 2400, 4000 SiC paper, using ethanol as a lubricant, rinsed with ethanol and dried in a stream of compressed air.

All electrolytes were prepared using analytical grade reagents (Sigma Aldrich) and Millipore water. The list of chemicals tested in this study as inhibitors is shown in **Table 2** (pK_a values are taken from [52–54]). Amount of the reagents, necessary to prepare 0.05 M solution, was added to 0.1 M NaCl solution and stirred until complete dissolution. The initial pH of Sal and Fum were 5.3 and 6.7 respectively; the pH of the commercial pyridinedicarboxylic acid was adjusted by 1M NaOH solution to the value of 5.5. All the experiments were also repeated in unbuffered 0.1 M NaCl solution without inhibitors for comparison.

For the interpretation of *in situ* Raman and IR spectra of Mg, the reference compounds listed in **Table 3** were prepared.

2.2. Hydrogen evolution measurements

Hydrogen evolution measurements were performed to calculate the inhibiting efficiency of the selected carboxylates. For this, the ground plates of CP-Mg342 and HP-Mg51 were placed in 0.1 M NaCl solution with and without the inhibitors. The surface area of each sample was measured and varied between 15.6 to 17.5 cm² while the reaction flask of contained 500 ml of the constantly stirred electrolyte. The commercial eudiometers (Neubert-Glas, Germany) combined with an electronic balances were used for a continuous automated recording of the weight of water displaced by the evolved hydrogen [55]. The values of the inhibiting efficiency (IE, %) were calculated as follows:

$$IE, \% = 100\% \times (V_{H_2}^{NaCl} - V_{H_2}^{Inh}) / V_{H_2}^{NaCl} \quad (1)$$

where $V_{H_2}^{NaCl}$ and $V_{H_2}^{Inh}$ are the normalized volume of hydrogen evolved in pure NaCl solution or NaCl containing 0.05M solution of corrosion inhibitor.

2.3. Raman spectroscopy

Raman spectra were recorded on Renishaw InVia Confocal Raman Microscope (CRM), using the green laser (doubled Nd:YAG, 532 nm) with the power of 50 mW. Objectives with $\times 5$ and $\times 20$ magnification were used to make the optical images of the sample surface. *In situ* Raman measurements were performed with Leica long working distance objective ($\times 50$, numerical aperture NA = 0.5).

The surface evolution was studied *in situ* and the kinetics of the surface film growth was measured using the methodology described in detail in [56], Kinetic Raman Mapping. Briefly, a freshly prepared Mg sample was mounted in a flow cell with the glass optical window (active surface 3.14 cm², electrolyte thickness ~ 1 mm). The H₂ bubbles coming from the water reduction reaction were continuously removed from the corroded surface by the solution flow. 25 ml of the used solution recirculated through the cell with the rate of 5 ml/min. Solution pH was continuously measured during the experiments. Initial neutral pH reached the values of 10 – 11 for 5-10 minutes of the experiment for all the solutions except PDC (it took 40 min in this case), which was used in acidic form.

Raman mapping was performed every 7 to 10 minutes during 2 hours on the areas of 100 \times 100 μm with the step of 10 μm . Two series of Raman spectra were recorded: in range of 100 - 1800 cm⁻¹ (typical for organic groups) and 2500 – 3800 cm⁻¹ (organic groups but also OH-groups). Exposure time was 0.2 sec for each location on the surface, the total time of each map recording was about 2 minutes.

The reference spectra of the inhibitors solutions were collected in saturated solutions. The used Raman set up was not able to detect the peaks of diluted solutions used for *in situ* experiments. *In situ* detected Raman bands of organic molecules could be hence attributed to the adsorbed molecules.

2.4. Attenuated Total Reflectance Fourier-Transform Infrared Spectroscopy (ATR-FTIR)

Infrared spectra were measured for both, dry and wet surfaces, using a Thermo Scientific Nicolet 6700 Fourier Transform Infrared (FTIR) spectrometer equipped with a mercury cadmium telluride detector cooled at 77 K by liquid nitrogen. The ATR accessory was a horizontal ZnSe crystal coated with diamond (A = 2.54 mm²) with single reflection and an angle of incidence of 45° (Smart Miracle from PIKE). The spectra were recorded with resolution 4 cm⁻¹ and were averaged from 256 scans. OMNIC software was used for the data collection and treatment.

The ATR spectra were recorded on the wet Mg surface after 2 h of exposure in a flow-cell with the studied electrolyte. The humid sample was pressed against the ATR crystal and the measurement was made. The spectrum of the unreacted electrolyte containing the inhibitor was used as the background, which is a standard procedure in adsorption studies aiming to detect only adsorbed species. No other correction was applied afterwards.

2.5. Glow Discharge Optical Emission Spectroscopy (GD-OES)

GD-OES analysis was performed with a GD-Profilier 2 (HORIBA Jobin Yvon) using Quantum software. The instrument configuration included a pulsed radiofrequency (RF) generator, a standard HJY glow discharge source with an anode of 4 mm internal diameter and an automatic impedance matching system between the RF generator and the GD source. Mixture of Ar with 10000 ppm of H₂ was prepared by Air Liquide and used as the discharge gas. The optical system was purged by high purity N₂ in order to detect emission lines in the UV region. The Differential Interferometry Profiling (DiP) system integrated in the instrument allowed a direct depth measurement along with the elemental depth analysis. Elemental depth profiling was performed under Ar/H₂ pressure of 750 Pa and a power of 17 W. The used spectral wavelengths were: Mg - 285.217 nm, C - 156.149 nm, Cl - 134.730 nm and O - 130.223 nm.

GD-OES depth profiling was performed on the samples after 30 min (in case of NaCl solution) or 2h (in case of inhibitors) of the electrolyte circulation in a flow-cell.

2.6. Scanning electron microscopy (SEM)

Field emission gun scanning electron microscope (FEG SEM) Hitachi SU-70 was used with an applied accelerating voltage of 15 kV and a working distance of 9 mm in secondary electron imaging mode. All samples were sputtered with a carbon layer for enhancing surface conductivity and eliminating charge effects on non-conductive regions.

SEM analysis was performed on CP-Mg342 samples after 30 min of the reaction with studied solutions in a flow cell. The solutions were recirculated with the rate of 5 ml/min. Solution residuals were flushed off from the sample surface with deionized water and the metal surface was dried in N₂ flow. The central area of the samples was chosen for the SEM investigation.

3. Results

3.1. Surface morphology and H₂ evolution

Fig. 1(a-f) illustrates the corroded surfaces after 2 hours of exposure in the flow cell with recirculating solution of 0.1 M NaCl, with and without the inhibitors. The high resolution optical images (right side of each figure) were taken *in situ* under the electrolyte flow. The general view of the surface is shown after the sample removal from the cell, in order to illustrate the difference between the corroded zones and zones which were not exposed to the electrolyte. For CP-Mg342, it is clear from **Fig.1a** that the surface is more attacked on the sample, which was in contact with the NaCl solution without inhibitors. **Fig. 1a** reveals the filiform-like corrosion, which looks like black threads of about 10 μm width (right part of the figure, with higher magnification). The surface which was in contact with

the inhibitor solutions (**Fig. 1 c, e, f**) has different appearance in comparison with the pristine area, however no filaments were detected after 2 hours, suggesting a partial corrosion protection.

For HP-Mg 51, no filaments were observed in any case, at least for 2 h of experiment (**Fig. 1 b, d**). In case of HP-Mg51, Sal acts as an etching agent revealing differently oriented grains (**Fig. 1d, right part**). As expected from the previous work, Sal accelerates corrosion of HP-Mg51, because the positive effect of Fe-binding (dominating in case of CP-Mg342) is negligible in comparison with the Mg^{2+} binding effect in Fe-deficient alloy ($\text{Log } K_{Fe(III)} = 36.8$ and $\text{Log } K_{Mg(II)} = 4.7$) [12]. In presence of Fum and PDC the surface looked similar to the surface of CP-Mg342 (**Fig. 1 e, f**), so it is not shown in this figure.

Described surface appearance is in good agreement with the hydrogen evolution curves (**Fig. 1 g**). HP-Mg51 showed much lower corrosion rate compared to that of CP-Mg342. The inhibiting efficiency (**Table 2**) of three carboxylates applied to CP-Mg342 varied between 84 to 89%, while it was lower when applied to HP-Mg51 (58% for Fum and 74% for PDC). Concomitantly, fitting the visually observed performance in **Fig. 1d**, Sal accelerated dissolution of HP-Mg51 exhibiting negative inhibiting efficiency of -244%.

The micrographs of CP-Mg342 ppm surface after 30 min of exposure to different solutions are shown in **Fig. 2**. All the micrographs were taken on the magnesium matrix, at least 20 μm away from coarse Fe-containing inclusions. After the exposure to the non-inhibited NaCl electrolyte, **Fig. 2a**, the surface is covered by rosettes consisting of well-defined $Mg(OH)_2$ platelets. After the contact with the Sal-containing solution (**Fig. 2b**) the surface film has a sponge-like morphology consisting of irregularly shaped lamellas with a thickness of about 50 nm and does not display well-defined platelets. The corrosion products formed in the solutions containing PDC (**Fig. 2c**) and Fum (**Fig. 2d**) display a network consisting of nanosheets with the average thickness of about 25 nm for Fum and less than 20 nm PDC respectively. In the former case, the cells of the network are much larger than in the latter case. Clearly, the morphology of corrosion product films formed in the presence of the inhibitors differs from the morphology of the film formed in the pure NaCl solution.

This difference in morphology is coherent with the expected strong effect of the synthesis conditions and precursors on the resulting morphology of Mg hydroxides [57]. By varying the synthesis conditions, sources of magnesium, surfactants, solvents, pH etc. it is possible to obtain platelet-, tube-, needle-, and lamella-like nanostructures. Interestingly, similar lamellar $Mg(OH)_2$ structures, as the presented in **Fig. 2 b, c, d**, were obtained on Mg metal in formamide / water mixture electrolytes at 80°C [58]. The observed structure has been ascribed to the binding of formamide molecules to magnesium atoms, which inhibited the growth of $Mg(OH)_2$ perpendicular to the (0 0 0 1) plane [58]. Organic inhibitors employed in this work may have similar tendency to adsorb onto the hydroxide surface and tailoring the surface morphology forming nanosheets and irregular particles (**Fig. 2b,c,d**). Nanoplatelets of $Mg(OH)_2$ crystals observed in (**Fig. 2a**) have very common shapes which

are typical for the products of many different Mg hydroxides produced with or without addition of various compounds [57].

3.2. Corrosion products growth detected by vibrational spectroscopy

In situ Raman spectra of all the samples demonstrated the typical for –OH vibrations in Mg(OH)₂ band at 3652 cm⁻¹ [59]. Spectra for both types of Mg showed similar tendencies (except HP-Mg51 in Sal solution, where Mg(OH)₂ was not detected at all), so only CP-Mg342 is presented in **Fig. 3a**. Additional small peaks at 3675 cm⁻¹ and 3710 cm⁻¹ appearing in the spectra in the presence of the inhibitors were attributed to the surface –OH groups of Mg(OH)₂ in our previous work [56]. The presence of these peaks in Raman spectra implies the well-developed surface and the smaller crystals compare to the sample exposed to the solution without inhibitors.

Mg(OH)₂ (bulk brucite) growth kinetics was estimated by the evolution of the 3652 cm⁻¹ peak area in *in situ* Raman spectra, after background suppression and the normalizing of the signal by the maximum of water band (3415 cm⁻¹), see [56] for more details. The peak area was calculated as it is shown in **Fig. 3a** (spectrum “without inhibitors”, the shaded zone between the spectrum and the baseline passing through 2 points on the spectrum with the abscissa 3640 and 3665 cm⁻¹). For HP Mg-51, the brucite peak was very small and its evolution did not exceed the precision of the measurement, making impossible to quantify the kinetics of the corrosion product growth. For commercial purity magnesium, Mg-342, the representative kinetics of the brucite growth on corroding Mg in different electrolytes is shown in **Fig. 3b**. As expected based on our previous results [56], Mg(OH)₂ growth is fitted by the linear law when exposed to pure NaCl solution. It is obvious from the comparison of the curves slopes, that Mg(OH)₂ growth rate is reduced by all the inhibitors and that the effect is different for different inhibitors. With Sal and PDC, during approximately 40 minutes Mg(OH)₂ growth rate seems not to be affected by the presence of the inhibitor but it decreases notably after 40 minutes, whereas in presence of Fum no induction period was noticed and Mg(OH)₂ growth rate is low from the very beginning of the experiment.

3.3. Carboxylate interaction with corroding Mg by vibrational spectroscopy

In situ Raman spectra and IR spectra in range of 750 – 1750 cm⁻¹ show the fingerprints of different functional groups typical for the organic inhibitors themselves (**Fig. 4-6 a**). *In situ* Raman spectra and IR spectra recorded on wet samples, just after the reaction with the studied solution were compared with the spectra of saturated inhibitors solutions and with different synthetic reference samples (**Table 3**) in order to conclude the specific interaction of inhibitors molecules with the sample surface or formation of soluble complexes.

Firstly, one should note that in case of Sal (CP-Mg342), the signal corresponding to organic molecules (750 – 1750 cm⁻¹) was detected by Raman spectroscopy after around 40

minutes of the experiment. This fact is in agreement with the $\text{Mg}(\text{OH})_2$ kinetics trend suggesting that the inhibiting action of Sal as well as slowing down of $\text{Mg}(\text{OH})_2$ growth starts at the same time. Secondly, marked shifts in band positions were discovered for CP-Mg342 compared to Sal solution and *in situ* spectra on HP-Mg51, indicating the strong chemical interaction with the surface of CP-Mg342 (**Fig. 4a**). Similar shifts in band position when compared with Sal solution spectra were noticed in IR spectra (**Fig. 4b**).

IR and Raman spectra of different reference compounds (wet powders of $\text{Mg}(\text{OH})_2$, $\text{Fe}(\text{OH})_3$, precipitated in presence of Cl^- and Sal from the corresponding chlorides by addition of NaOH, Fe(III) complex with Sal and carbon steel immersed in Sal solution for 2 hours) were also recorded. Comparing the observed Raman shifts with the shifts obtained on the reference samples we could attribute the most of the bands positions on CP-Mg342 to the $\text{Mg}(\text{OH})_2$ precipitated in presence of Sal (**Fig. 4**). However, some additional shifts matched well with the positions corresponding to the most intensive peaks of Fe(III)Sal complex (**Fig. 4**). Detailed peaks positions and assignments are presented in **Table 4** (bands assignment was based on [38,40,60–64]). These results imply the Sal adsorption on the precipitated hydroxide and formation of soluble complex with Fe(III) incorporated in the corrosion products.

Raman spectra recorded on both Mg samples in presence of PDC solution didn't reveal any difference in band position as compared with the spectra of PDC solution during the first 40 min (**Fig. 5a**, only CP-Mg342 is shown). However, the intense fluorescent background appeared after 40 min (the time corresponding to the time of the modification of the brucite growth kinetics) so that the Raman signals were impossible to observe at the end of experiment. In contrast, IR spectra recorded after exposure to the flow-cell demonstrate some differences as compared to the spectrum of PDC solution (see **Table 5**, **Fig. 5b**, [65–68]). Band at 1724 cm^{-1} , attributed to C=O stretching vibration appears on spectra of wet Mg sample; bands in range of $1580 - 1610\text{ cm}^{-1}$ attributed to asymmetric stretching modes of COO^- groups [66,67] are shifted. Nevertheless, position of symmetric modes of COO^- (stretching at 1362 and 1385 , bending at 826 cm^{-1}) remains the same. Bending mode of aromatic system (1030 cm^{-1}) is shifted towards higher wavenumbers compared to solution spectrum.

No shifts if compared to the Fum solution were noticed in Raman spectra recorded on both Mg samples in presence of Fum (**Fig. 6a**, only CP-Mg342 is shown). IR spectra of both Mg samples demonstrate insignificant shifts compare to spectrum of Fum solution (see **Table 6** and **Fig. 6b**, [69,70]). Additional shoulder at 1395 cm^{-1} , which is absent in spectrum of Fum solution and assigned as symmetric stretching vibration of COO^- groups appears on spectrum of Mg samples. Additionally, a slight broadening of the band at 1569 cm^{-1} was observed. These two shoulders might be attributed to symmetric and asymmetric stretches of the carboxylate bonds and indicate chemisorption of Fum.

3.4. Elemental depth distribution of corroded surfaces from GD-OES

Fig. 7 illustrates the elemental depth profiles of C, O, Mg and Cl, obtained for the samples of CP-Mg342 corroded in absence and in presence of the inhibitors (depth profiles of HP-Mg51 had the same tendency, so only Mg-342 profiles are shown).

Generally, the interface between the metal and the oxide/hydroxide layer is defined by the inflection (decrease) of the oxygen and inflection (increase) of magnesium signal between 25 and 75 % of the maximal intensity. For the reference sample exposed in 0.1 NaCl solution without inhibitors, we had to reduce the exposure time in order to avoid the formation of too porous and rough surface, which is not suitable for GD-OES; therefore, the oxide/hydroxide layer seems thinner than for the other samples. The thickness of the oxide layer formed during 2 hours of the exposure in the solutions containing inhibitors correlates well with the kinetics data obtained by *in situ* Raman spectroscopy: the oxide layer for Fum is the thinnest among the studied samples.

It should be noted, that the intensity of any element does not provide the information about its mass without a calibration procedure. However, for our purposes it is sufficient to compare the profiles of the similar samples and estimate the preferential presence of a particular element qualitatively. It can be seen from the figure, that the intensity of Mg as the principal element is similar within the oxide layer (and in the bulk) for all the samples, making possible to assume similar emission efficiency during erosion of different samples for other elements and to compare the relative intensity of all elements between the samples.

It is clear from **Fig. 7a** that without inhibitors the oxide/hydroxide layer is enriched by Cl. Since no Na was detected in the oxide/hydroxide layer (not shown), most probably, the Cl presence in the surface film corresponds to Cl⁻ anions adsorption on positively charged Mg(OH)₂ [71]. Depth profiles of the samples exposed in flow cell in presence of inhibitors demonstrate carbon enrichment in the oxide layer, indicating the presence of the organic molecules in the surface film. Interestingly, the carbon distribution in the oxide layer varies between the samples exposed in the solutions of different inhibitors. For Sal, the carbon level is much higher as compared to other inhibitors. For PDC, carbon signal reaches the maximum within the oxide/hydroxide layer while it seems that the carbon-containing layer separates two different oxidized layers: O and Mg signals are evolving in two steps (**Fig. 7c**).

4. Discussion

4.1. General features of Mg corrosion in presence of carboxylates

It is commonly accepted that Mg reactivity strongly depends on two factors: barrier properties of the surface film and distribution of more noble impurities in Mg matrix [72].

Considering the surface film itself, its hydrophobic properties, crystal morphology and crystal size can play an important role in barrier protection. Access of water and diffusion of aggressive species to the metal substrate through the layer consisting of the large crystals with low surface area is easier than in case of the compact layer. The low fraction of brucite compared to the inner MgO can also indicate the stabilization of the inner oxide [73].

The second factor playing an important role in Mg reactivity is the presence of Fe-rich inclusions in Mg matrix. The detrimental effect of Fe (along with other transition metals like Ni and Cu) has also been repeatedly reported by multiple authors starting from as early as 1942 [12,50,74,75]. The role of more noble than Mg inclusions is usually associated with the formation of microgalvanic cells between the inclusion and Mg matrix, where the inclusion acts as a local cathode, accelerating H₂ evolution and material degradation. Influence of Fe content is obvious from difference in the corrosion rate for HP-Mg51 and CP-Mg220 containing 51 and 220 ppm of Fe respectively reported previously [12] and evidenced in this work by the surface appearance of corroded samples and H₂ evolution for HP-Mg51 and CP-Mg342 containing 51 and 342 ppm Fe (**Fig. 1**), showing that after 24 hours of immersion, the corrosion rate of CP-Mg342 is twenty times higher than that of HP-Mg51 (**Fig. 1g**).

Thus, further discussion of inhibition mechanisms of three investigated carboxylates is based on explanation of how the inhibiting species influence both of these factors: surface film growth and interaction with Fe-riched inclusions.

Firstly, the common effect of all studied carboxylates is the formation of more compact layer of Mg(OH)₂ (as compared with the reference NaCl solution), which limits the access of solution to the metal interface and Cl⁻ adsorption due to the repulsion effect of the organic molecules with high electron density. Formation of the surface film with more compact morphology was evidenced by SEM images (**Fig. 2**). *In situ* Raman spectra in range of -OH vibrations (**Fig. 3a**, satellite peaks at 3675 and 3710 cm⁻¹, attributed to the surface -OH groups) also supported the hypothesis of formation of smaller crystals with well-developed surface in presence of organic molecules. GD-OES profiles showed much lower content of Cl in the oxidized layer (**Fig. 7 b-d**) and higher content of C, supporting the competitive adsorption of organic molecules on the surface film. However, the reason of such an effect, most probably, is different for various inhibitors, according to other results (shifts of peaks position in Raman and IR spectra, Mg(OH)₂ growth kinetics, carbon depth distribution in GD-OES profiles). Therefore, each carboxylate is discussed separately.

4.2. Dual action of sodium salicylate (Sal) on Mg corrosion

First of all, the accumulation of Sal molecules on corroded surface of CP-Mg342 sample (C signal in GD-OES depth profile, **Fig. 7**), was significantly higher than for others inhibitors. According to Raman and IR spectra of CP-Mg342 sample exposed in Sal solution (**Fig. 4**), this accumulation can be assigned to a chemical adsorption of Sal. Significant shifts

in bands position as compared with Sal solution spectra, suggested the modification of Sal molecule geometry caused by strong interaction between Sal and the surface. According to the shifts of COO^- (in Raman spectra: 1605, 1575, 1393, 821 cm^{-1}) and $-\text{OH}$ (1252 cm^{-1}) bands, both of these groups participate in the interaction [38]. Comparison with the reference samples demonstrated that the most of the shifts can be explained by the interaction with $\text{Mg}(\text{OH})_2$. Indeed, Sal is known as an agent stabilizing the nano-particles of metal oxides or hydroxides due to the adsorption on their surface [39]. The fact that Sal inhibits corrosion of CP-Mg342 and accelerates HP-Mg51 is also coherent with Sal stabilization on $\text{Mg}(\text{OH})_2$ layer. Initial reactivity of CP-Mg342 is higher as compared to HP-Mg51 due to the presence of significant amount of Fe inclusions [12], therefore $\text{Mg}(\text{OH})_2$ precipitates very fast, as confirmed by *in situ* growth kinetics. Hence, Sal is able to adsorb on the freshly formed hydroxide. In contrast, HP-Mg51 corrodes slowly, so Sal interacts with metallic Mg (or the surface oxide which is every time present on Mg), promoting its fast dissolution, which is similar to the effect of Sal reported for metallic iron and oxidized iron surface [22,35–40].

Additional shifts, different from those observed on $\text{Mg}(\text{OH})_2$ precipitated in the presence of Sal, were however observed in vibrational spectra of CP-Mg342 sample but not for HP Mg51 sample exposed in Sal containing solutions; namely the peak at 1605 cm^{-1} , broad peak at 1317 cm^{-1} for Raman spectra and broad band at 1531 cm^{-1} in IR spectra. The apparent bands position shift in vibrational spectra can be explained by assuming two distinct species with fixed absorption frequencies, which vary only their population and consequently their relative intensities, which can be caused by the effect of temperature or concentration [76,77]. In our case, all the measurements were done on the same instrument and at the same temperature. The effect of concentration can eventually take place, because the surface area (area of adsorption sites) of precipitated $\text{Mg}(\text{OH})_2$ might be not the same as on corroded Mg sample. However, the difference between the spectra of CP-Mg 342 sample and HP Mg51 sample in the region relevant for the organic groups, leads us to an alternative explanation of the shifts in vibrational spectra. We suggest that the shifts are related to the presence of soluble Fe-Sal complex in the surface layer, given the coincidence of these shifts with the most intensive characteristic peaks of Fe(III)-Sal soluble complex for both, IR and Raman spectra (**Fig. 4**). This suggests that besides the stabilization of $\text{Mg}(\text{OH})_2$ nano-crystals, Sal inhibition efficiency can be related to the binding of Fe ions coming from dissolution of detached from Mg substrate Fe-rich particles. This prevents iron re-deposition and inhibits cathodic reaction. This mechanism is in agreement with the data reported in the literature [12,49,51] suggesting the cathodic type of inhibition by Sal, as well as with the absence of the inhibiting effect on HP-Mg51 sample, poor in active iron-rich intermetallic particles. Apart from complexing Fe^{3+} ($\text{Log } K_{\text{Fe(III)}} = 36.8$), Sal forms stable complexes with Mg^{2+} ($\text{Log } K_{\text{Mg(II)}} = 4.7$ [78]). Given this, the positive effect of iron complexing, outweighing in case of CP-Mg342, is offset by accelerated Mg dissolution in case of Fe-poor HP-Mg51.

Kinetics of $\text{Mg}(\text{OH})_2$ growth on CP-Mg342 in presence of Sal is described by a two steps trend (**Fig. 2b**): the first 40 minutes it evolves like in solution without inhibitor (step

1), and then the growth rate of $\text{Mg}(\text{OH})_2$ slows down (step 2). H_2 evolution (**Fig.1g**, CP-Mg342) demonstrates a similar two-steps tendency as $\text{Mg}(\text{OH})_2$ growth, even if the time of the transition is not exactly the same as in the *in situ* Raman experiments. Such a big difference in the transition time can be explained by the difference in the experimental set up, impacting the ratio between the active surface and the solution volume. Step 1 (40 min in case of Raman experiments and around 6 h in case of H_2 evolution measurements) corresponds probably to the time needed to dissolve the Fe-containing particles and stabilize the formation of $\text{Mg}(\text{OH})_2$ particles with well-developed surface. Thus, the inhibition effect (Step 2) of Sal starts only after this “induction period”.

To sum up, it is likely that the inhibition efficiency of Sal can be explained by both Fe-complexing and stabilization of $\text{Mg}(\text{OH})_2$ nano-crystals due to the strong chemical interaction with the surface. The proposed mechanism is schematically presented in **Fig. 8**.

4.3. Coordination polymer film formation by 2,5-pyridinedicarboxylate (PDC)

For PDC, GD-OES profile differs significantly from those of other inhibitors (**Fig. 7c**). During the sputtering of the oxide/hydroxide layer, intensities of all elements evolve in two steps. This fact could be explained by formation of two distinct layers with different sputtering rate. Probably, it corresponds to the inner layer of $\text{MgO}/\text{Mg}(\text{OH})_2$ and the outer layer of MgPDC . Carbon intensity reaches the maximum at the interface between these two layers, suggesting the enhanced accumulation of PDC molecules there.

Secondly, the high fluorescence background appears in Raman spectra of CP-Mg342 after an “induction period” of 40 min, as it was mentioned in section 3.2. PDC molecule itself does not provide fluorescence background, as evidenced by Raman spectrum of PDC solution (**Fig. 5a**). However, formation of a specific network of the organic molecules which contains a chain of alternating double and single bonds, called conjugation, or π -electron delocalization can cause fluorescence [79,80]. It was reported that PDC can form so-called coordination polymer with different dimensionality, consisting of the long chains of PDC molecules bonded due to the electrostatic interaction with metal ions [80–82]. Many of reported coordination polymers have fluorescent properties [46,80,83].

Analysis of IR spectra of CP-Mg342 (**Fig. 5b**) demonstrated that bands of carboxylates (COO^-) were shifted as compared to the solution spectra (1607 - ν_{as} , 1457 - ν_{s} [68]). Band at 1724 cm^{-1} corresponding to $\text{C}=\text{O}$ stretching of COOH , is absent in the PDC solution spectrum and appears in the spectrum of Mg sample, suggesting that the delocalization of electron density of carboxylic group disappears, instead the $-(\text{C}=\text{O})-\text{O}^-$ is taking place; which can be schematically illustrated by a mechanism shown in **Fig. 9**.

$\nu(\text{C}=\text{C})$ and $\nu(\text{C}=\text{N})$ vibrations in PDC solution at 1581 and 1030 cm^{-1} are shifted to higher wavenumbers on Mg sample spectra (1589 and 1036 cm^{-1}). Therefore, most likely the coordination occurs through both, COO^- group and pyridine N [83] The proposed structure of PDC complex is presented in **Fig. 9**.

As it was described in Section 2.1, PDC was prepared from PDCA by the addition of NaOH and pH adjustment to ≈ 5 . It means that one of the COOH group can be still protonated at the very beginning of experiment ($pK_{a2} = 4.64$, which is close to experimental value of pH). Thus, the “induction period” of 40 min in kinetics curve of $Mg(OH)_2$ growth can be related either to the period which is necessary for increasing pH [80] and formation of the polymer film or to the time necessary to accumulate sufficient amount of Mg^{2+} to precipitate coordination polymer.

To summarize, precipitation of coordination polymer consisted of long chains of PDC molecules bonded due to the electrostatic interaction with metal cations is the possible explanation of Mg corrosion inhibition by PDC, as schematically illustrated in **Fig. 9**. If such a film is formed, the inhibitor affects both, cathodic and anodic reactions, and hence acts as a mixed type inhibitor. Similarly, conclusion about the mixed inhibiting behavior (with more pronounced anodic inhibition) of related 2,5-PDC was drawn in our previous paper [51].

4.4. Adsorption of Fumarate (Fum) on corroding Mg

Despite the well-developed $Mg(OH)_2$ surface, accumulation of Fum on corroding Mg is relatively low as compared to other inhibitors: in GD-OES depth profiles of CP-Mg342 (**Fig. 7**), the intensity of C within the oxide layer is lower than in the oxide layers formed in the presence of other inhibitors but it is still higher than for the bulk indicating the presence of organic molecules.

In situ Raman spectra in the range of $700 - 1700\text{ cm}^{-1}$ (**Fig. 6a**) do not allow to detect any significant shifts as compared with Fum solution, indicating that the interaction is weak and does not modify significantly the geometry of the adsorbed molecule [84]. In contrast, the *ex situ* IR spectrum of Fum on CP-Mg342 (**Fig. 6b**) demonstrates a shoulder at 1395 cm^{-1} in addition to the main band at 1372 cm^{-1} . This shoulder could be assigned to a carboxylate group chemically interacting with the surface, as was observed for fumarate adsorbed on TiO_2 [85], acetate on TiO_2 [85], benzoate on quartz [86], laurate on alumina [86], oxalate and malonate on metal (oxy)hydroxides [87]. The separation of the adsorption bands corresponding to the carboxylate antisymmetric and symmetric stretching can be used to speculate on the mode of coordination [76]. For the shoulder at 1395 cm^{-1} the separation is around 174 cm^{-1} , which could be interpreted as a bridging bidentate surface complex (both oxygen atoms of one carboxylate group participate in bonding, as schematically illustrated in **Fig. 10**). However, our results are not sufficient to conclude if both COO- groups of Fum or only one of them participate in adsorption. Additional study is also necessary to elucidate the orientation of the adsorbed carboxylate groups of fumarate.

Conclusions

Surface analysis techniques such as *in situ* Raman spectroscopy in kinetic mapping mode, ATR-FTIR and GD-OES were applied to study the effect of selected carboxylates (Sal, Fum and PDC) on the surface film formation and evolution during corrosion of pure Mg in aqueous solutions containing Cl⁻. Namely, the growth kinetics of the surface film, its chemical composition, depth elemental distribution and morphology were studied.

Raman spectra in the range of -OH vibrations as well as SEM images demonstrated that addition of all of these inhibitors results in the decrease of the size of Mg(OH)₂ crystals in the corrosion products layer. GD-OES elemental depth profiles demonstrated that Cl⁻ accumulation and diffusion through the oxidized layer were efficiently prevented.

Three different film formation mechanisms, relevant for inhibition, were proposed: adsorption of Fum on the metallic Mg surface or MgO, stabilization of Mg(OH)₂ particles due to the chemical adsorption of Sal and precipitation of coordination polymer at the interface between more and less hydrated oxide layers in case of PDC. Characteristic peaks of soluble Fe(III)Sal complex have been found in the spectra of CP-Mg342 sample corroded in presence of Sal, thus Fe-complexing mechanism more likely takes place in case of Sal inhibition. This mechanism is also consistent with the fact that Sal only inhibits corrosion of CP-Mg342 with high Fe content and was previously described as cathodic inhibitor.

A.M. - Data curation; Formal analysis; Investigation; Methodology; Validation; Visualization; Writing – original draft; Writing – review & editing

S.L.- Resources; Supervision; Validation; Visualization; Writing – review & editing.

K.Y.- Investigation; Validation; Visualization; Writing – review & editing.

D.M.- Investigation; Validation; Visualization.

D.K.- Investigation; Validation; Visualization; Writing – original draft.

M.Z.- Project administration; Resources; Writing – review & editing.

G.L. -Investigation; Methodology; Supervision; Formal analysis; Writing – review & editing.

P.V. – Conceptualization, Methodology, Visualization; Project administration; Funding acquisition; Supervision; Writing – original draft; Writing – review & editing.

Declaration of interests

The authors declare that they have no known competing financial interests or personal relationships that could have appeared to influence the work reported in this paper.

Acknowledgements

KY thanks Researcher grant (IF/01284/2015) and Project CICECO-Aveiro Institute of Materials, FCT Ref. UID/CTM/50011/2019, financed by national funds through the FCT/MCTES and co-financed by FEDER under the PT2020 Partnership Agreement.

References:

- [1] D. Schloffer, S. Bozorgi, P. Sherstnev, C. Lenardt, B. Gollas, Manufacturing and characterization of magnesium alloy foils for use as anode materials in rechargeable magnesium ion batteries, *J. Power Sources*. 367 (2017) 138–144. doi:10.1016/j.jpowsour.2017.09.062.
- [2] H. Hornberger, S. Virtanen, A.R. Boccaccini, Biomedical coatings on magnesium alloys - A review, *Acta Biomater.* 8 (2012) 2442–2455. doi:10.1016/j.actbio.2012.04.012.
- [3] Y. Zhang, J. Xu, Y.C. Ruan, M.K. Yu, M. O’Laughlin, H. Wise, D. Chen, L. Tian, D. Shi, J. Wang, S. Chen, J.Q. Feng, D.H.K. Chow, X. Xie, L. Zheng, L. Huang, S. Huang, K. Leung, N. Lu, L. Zhao, H. Li, D. Zhao, X. Guo, K. Chan, F. Witte, H.C. Chan, Y. Zheng, L. Qin, Implant-derived magnesium induces local neuronal production of CGRP to improve bone-fracture healing in rats, *Nat. Med.* 22 (2016) 1160–1169. doi:10.1038/nm.4162.
- [4] J. Gonzalez, R.Q. Hou, E.P.S. Nidadavolu, R. Willumeit-Römer, F. Feyerabend, Magnesium degradation under physiological conditions – Best practice, *Bioact. Mater.* 3 (2018) 174–185. doi:10.1016/j.bioactmat.2018.01.003.
- [5] M.A. Deyab, Decyl glucoside as a corrosion inhibitor for magnesium-air battery, *J. Power Sources*. 325 (2016) 98–103. doi:10.1016/j.jpowsour.2016.06.006.
- [6] F.W. Richey, B.D. McCloskey, A.C. Luntz, Mg Anode Corrosion in Aqueous Electrolytes and Implications for Mg-Air Batteries, *J. Electrochem. Soc.* 163 (2016) A958–A963. doi:10.1149/2.0781606jes.
- [7] M. Deng, D. Höche, S. V. Lamaka, D. Snihirova, M.L. Zheludkevich, Mg-Ca binary alloys as anodes for primary Mg-air batteries, *J. Power Sources*. 396 (2018) 109–118. doi:10.1016/j.jpowsour.2018.05.090.
- [8] D. Höche, S. V. Lamaka, B. Vaghefinazari, T. Braun, R.P. Petruskas, M. Fichtner, M.L. Zheludkevich, Performance boost for primary magnesium cells using iron complexing agents as electrolyte additives, *Sci. Rep.* 8 (2018) 1–9. doi:10.1038/s41598-018-25789-8.
- [9] M. Yuasa, X. Huang, K. Suzuki, M. Mabuchi, Y. Chino, Discharge properties of Mg-Al-Mn-Ca and Mg-Al-Mn alloys as anode materials for primary magnesium-air batteries, *J. Power Sources*. 297 (2015) 449–456. doi:10.1016/j.jpowsour.2015.08.042.
- [10] S. V. Lamaka, J. Gonzalez, D. Mei, F. Feyerabend, R. Willumeit-Römer, M.L. Zheludkevich, Local pH and its Evolution near Mg Alloy Surfaces Exposed to Simulated Body Fluids, *Adv. Mater. Interfaces*. 1800169 (2018) 1–6. doi:10.1002/admi.201800169.
- [11] X.-P. Guo, G.-L. Song, J.-Y. Hu, D.-B. Huang, Corrosion inhibition of magnesium (Mg) Alloys, in:

- Corros. Prev. Magnes. Alloy., Elsevier, 2013: pp. 61–84. doi:10.1533/9780857098962.1.61.
- [12] S. V. Lamaka, B. Vaghefiazari, D. Mei, R.P. Petrauskas, D. Höche, M.L. Zheludkevich, Comprehensive screening of Mg corrosion inhibitors, *Corros. Sci.* 128 (2017) 224–240. doi:10.1016/j.corsci.2017.07.011.
- [13] G. Williams, R. Grace, R.M. Woods, Inhibition of the localized corrosion of Mg alloy AZ31 in chloride containing electrolyte, *Corrosion*. 71 (2015) 184–198. doi:10.5006/1376.
- [14] N. Dang, Y.H. Wei, L.F. Hou, Y.G. Li, C.L. Guo, Investigation of the inhibition effect of the environmentally friendly inhibitor sodium alginate on magnesium alloy in sodium chloride solution, *Mater. Corros.* 66 (2015) 1354–1362. doi:10.1002/maco.201408141.
- [15] J. Twu, P.K. Dutta, Raman-Spectroscopic Studies of Intercalated Molybdate Ions in Layered Metal-Hydroxides, *Chem. Mater.* 4 (1992) 398–401. doi:10.1021/cm00020a031.
- [16] N. Birbilis, G. Williams, K. Gusieva, A. Samaniego, M.A. Gibson, H.N. McMurray, Poisoning the corrosion of magnesium, *Electrochem. Commun.* 34 (2013) 295–298. doi:10.1016/j.elecom.2013.07.021.
- [17] R.L. Liu, M.F. Hurley, A. Kvrlyan, G. Williams, J.R. Scully, N. Birbilis, Controlling the corrosion and cathodic activation of magnesium via microalloying additions of Ge, *Sci. Rep.* 6 (2016) 1–12. doi:10.1038/srep28747.
- [18] D. Eaves, G. Williams, H.N. McMurray, Inhibition of self-corrosion in magnesium by poisoning hydrogen recombination on iron impurities, *Electrochim. Acta.* 79 (2012) 1–7. doi:10.1016/j.electacta.2012.05.148.
- [19] Z. Feng, B. Hurley, M. Zhu, Z. Yang, J. Hwang, R. Buchheit, Corrosion Inhibition of AZ31 Mg Alloy by Aqueous Selenite (SeO_3^{2-}), *J. Electrochem. Soc.* 166 (2019) C520–C529. doi:10.1149/2.0911914jes.
- [20] G. Boisier, A. Lamure, N. Pébère, N. Portail, M. Villatte, Corrosion protection of AA2024 sealed anodic layers using the hydrophobic properties of carboxylic acids, *Surf. Coatings Technol.* 203 (2009) 3420–3426. doi:10.1016/j.surfcoat.2009.05.008.
- [21] K. Khanari, M. Finšgar, M. Knez Hrnčič, U. Maver, Ž. Knez, B. Seiti, Green corrosion inhibitors for aluminium and its alloys: A review, *RSC Adv.* 7 (2017) 27299–27330. doi:10.1039/c7ra03944a.
- [22] Y.I. Kuznetsov, Organic corrosion inhibitors: Where are we now? A review. part III. Passivation and the role of the chemical structure of organophosphates, *Int. J. Corros. Scale Inhib.* 6 (2017) 209–239. doi:10.17675/2305-6894-2017-6-3-1.
- [23] M. Ormellese, L. Lazzari, S. Goidanich, G. Fumagalli, A. Brenna, A study of organic substances as inhibitors for chloride-induced corrosion in concrete, *Corros. Sci.* 51 (2009) 2959–2968. doi:10.1016/j.corsci.2009.08.018.
- [24] B. Lin, Y. Zuo, Corrosion inhibition of carboxylate inhibitors with different alkylene chain lengths on carbon steel in an alkaline solution, *RSC Adv.* 9 (2019) 7065–7077. doi:10.1039/C8RA10083G.
- [25] J. Wysocka, M. Cieslik, S. Krakowiak, J. Ryl, Carboxylic acids as efficient corrosion inhibitors of aluminium alloys in alkaline media, *Electrochim. Acta.* 289 (2018) 175–192. doi:10.1016/j.electacta.2018.08.070.
- [26] G. Žerjav, I. Milošev, Carboxylic acids as corrosion inhibitors for Cu, Zn and brasses in simulated urban rain, *Int. J. Electrochem. Sci.* 9 (2014) 2696–2715.
- [27] N. Dinodi, A.N. Shetty, Alkyl carboxylates as efficient and green inhibitors of magnesium alloy ze41 corrosion in aqueous salt solution, *Corros. Sci.* 85 (2014) 411–427. doi:10.1016/j.corsci.2014.04.052.
- [28] D. Daloz, C. Rapin, P. Steinmetz, G. Michot, Corrosion Inhibition of Rapidly Solidified Mg-3% Zn-15% Al Magnesium Alloy with Sodium Carboxylates, *Corrosion*. 54 (1998) 444–450. doi:10.5006/1.3284872.
- [29] I. V. Chernyshova, S. Ponnurangam, P. Somasundaran, Adsorption of fatty acids on iron (hydr)oxides from aqueous solutions, *Langmuir*. 27 (2011) 10007–10018. doi:10.1021/la2017374.
- [30] U. Rammelt, S. Koehler, G. Reinhard, Electrochemical characterisation of the ability of dicarboxylic acid salts to the corrosion inhibition of mild steel in aqueous solutions, *Corros. Sci.* 53 (2011) 3515–3520. doi:10.1016/j.corsci.2011.06.023.
- [31] F. Wormwell, A.D. Mercer, Sodium benzoate and other metal benzoates as corrosion-inhibitors in

- water and in aqueous solutions, *J. Appl. Chem.* 2 (2007) 150–160. doi:10.1002/jctb.5010020307.
- [32] L. Hamadi, S. Mansouri, K. Oulmi, A. Kareche, The use of amino acids as corrosion inhibitors for metals: A review, *Egypt. J. Pet.* 27 (2018) 1157–1165. doi:10.1016/j.ejpe.2018.04.004.
- [33] E.A. Batista, M.L.A. Temperini, An in situ SERS and FTIRAS study of salicylate interaction with copper electrode, *J. Solid State Electrochem.* 11 (2007) 1559–1565. doi:10.1007/s10008-007-0357-6.
- [34] M.A. Blesa, A.D. Weisz, P.J. Morando, J.A. Salfity, G.E. Magaz, A.E. Regazzoni, The interaction of metal oxide surfaces with complexing agents dissolved in water, *Coord. Chem. Rev.* 196 (2000) 31–63. doi:10.1016/S0010-8545(99)00005-3.
- [35] D. Eurof Davies, Q.J.M. Slaiman, Throughout the present investigation pure Fe supplied by the British Iron and, *Corros. Sci.* 11 (1971) 671–682.
- [36] D. Eurof Davies, Q.J.M. Slaiman, Mechanism of the corrosion inhibition of iron by sodium benzoate-III. The role of oxygen, *Corros. Sci.* 13 (1973) 891–905. doi:10.1016/S0010-938X(73)80071-X.
- [37] B.M. Vinoda, J. Manjanna, Dissolution of iron in salicylic acid and cation exchange between Fe(II)-salicylate and Na-montmorillonite to form Fe(II)-montmorillonite, *Appl. Clay Sci.* 97–98 (2014) 78–83. doi:10.1016/j.clay.2014.05.005.
- [38] M. V. Blber, W. Stumm, An In-Situ ATR-FTIR Study: The Surface Coordination of Salicylic Acid on Aluminum and Iron(III) Oxides, *Environ. Sci. Technol.* 28 (1994) 763–768. doi:10.1021/es00054a004.
- [39] I.L. Ardelean, L.B.N. Stoencea, D. Ficai, A. Ficai, R. Trusca, B.S. Vasile, G. Nechifor, E. Andronescu, Development of Stabilized Magnetite Nanoparticles for Medical Applications, *J. Nanomater.* 2017 (2017). doi:10.1155/2017/6514659.
- [40] E.C. Yost, M.I. Tejedortejedor, M.A. Anderson, Insitu CIR-FTIR characterization of salicylate complexes at the goethite/aqueous solution interface, *Environ. Sci. Technol.* 24 (1990) 822–828. doi:10.1021/es00076a005.
- [41] A. Alamdari, M.R. Rahimpour, N. Esfandiari, E. Nourafkan, Kinetics of magnesium hydroxide precipitation from sea bittern, *Chem. Eng. Process. Process Intensif.* 47 (2008) 215–221. doi:10.1016/j.cep.2007.02.012.
- [42] J.A. Dirksen, T.A. Ring, Fundamentals of Crystallization: Kinetic Effects on Particle Size Distributions and Morphology, *Chem. Eng. Sci.* 46 (1991) 2389–2427. doi:10.1016/0009-2509(91)80035-W.
- [43] T. Behrsing, G.B. Deacon, P.C. Junk, The chemistry of rare earth metals, compounds, and corrosion inhibitors, in: *Rare Earth-Based Corros. Inhib.*, Woodhead Publishing Series in Metals and Surface Engineering, 2014: pp. 1–37. doi:10.1533/9780857093585.1.
- [44] M. Forsyth, C.M. Forsyth, K. Wilson, T. Behrsing, G.B. Deacon, ATR characterisation of synergistic corrosion inhibition of mild steel surfaces by cerium salicylate, *Corros. Sci.* 44 (2002) 2651–2656. doi:10.1016/S0010-938X(02)00024-0.
- [45] M. Forsyth, B. Hinton, *Rare Earth-Based Corrosion Inhibitors*, Woodhead Publishing, 2015. doi:10.1016/C2013-0-16231-9.
- [46] R.K. Vakiti, B.D. Garabato, N.P. Schieber, M.J. Rucks, Y. Cao, C. Webb, J.B. Maddox, A. Celestian, W. Pan, B. Yan, Synthesis and Characterization of Two- and Three-Dimensional Calcium Coordination Polymers Built with Benzene-1,3,5-tricarboxylate and/or Pyrazine-2-carboxylate, *Cryst. Growth Des.* 12 (2012) 3937–3943. doi:10.1021/cg3003349.
- [47] N. Singh, P. Vishnoi, G. Anantharaman, Coordination polymers based on copper carboxylates and angular 2,5-bis(imidazol-1-yl)thiophene (thim2) ligand: Sequential structural transformations, *CrystEngComm.* 17 (2015) 2153–2161. doi:10.1039/c4ce02428a.
- [48] H. Wu, H.Y. Liu, J. Yang, B. Liu, J.F. Ma, Y.Y. Liu, Y.Y. Liu, Series of coordination polymers based on different carboxylates and a tri(4-imidazolylphenyl)amine ligand: Entangled structures and photoluminescence, *Cryst. Growth Des.* 11 (2011) 2317–2324. doi:10.1021/cg200005q.
- [49] S. V. Lamaka, D. Höche, R.P. Petruskas, C. Blawert, M.L. Zheludkevich, A new concept for corrosion inhibition of magnesium: Suppression of iron re-deposition, *Electrochem. Commun.* (2015). doi:10.1016/j.elecom.2015.10.023.
- [50] D. Höche, C. Blawert, S. V. Lamaka, N. Scharnagl, C. Mendis, M.L. Zheludkevich, The effect of

- iron re-deposition on the corrosion of impurity-containing magnesium, *Phys.Chem.Chem.Phys.* 18 (2015) 1279–1291. doi:10.1039/c5cp05577f.
- [51] J. Yang, C. Blawert, S. V. Lamaka, K.A. Yasakau, L. Wang, D. Laipple, M. Schieda, S. Di, M.L. Zheludkevich, Corrosion inhibition of pure Mg containing a high level of iron impurity in pH neutral NaCl solution, *Corros. Sci.* 142 (2018) 222–237. doi:10.1016/j.corosci.2018.07.027.
- [52] A.E. Martell, R.M. Smith, *Critical Stability Constants, Other organic ligands, V.3*, Springer, New York, 1977. doi:10.1007/978-1-4757-1568-2.
- [53] A.E. Martell, R.M. Smith, *Critical stability constants, Aminoacids, V. 1*, Springer, New York, 1974.
- [54] A.E. Martell, R.M. Smith, *Critical Stability Constants: Second Supplement*, Springer Science & Business Media, 1989. doi:10.1007/978-1-4615-6761-5.
- [55] D. Mei, S. V. Lamaka, C. Feiler, M.L. Zheludkevich, The effect of small-molecule bio-relevant organic components at low concentration on the corrosion of commercially pure Mg and Mg-0.8Ca alloy: An overall perspective, *Corros. Sci.* 153 (2019) 258–271. doi:10.1016/j.corosci.2019.03.039.
- [56] A. Maltseva, V. Shkirskiy, G. Lefèvre, P. Volovitch, Effect of pH on Mg(OH)₂ film evolution on corroding Mg by in-situ Kinetic Raman Mapping (KRM), *Corros. Sci.* 153 (2019) 272–282. doi:10.1016/j.corosci.2019.03.024.
- [57] G. Balducci, L. Bravo Diaz, D.H. Gregory, Recent progress in the synthesis of nanostructured magnesium hydroxide, *CrystEngComm.* 19 (2017) 6067–6084. doi:10.1039/c7ce01570d.
- [58] G. Zou, R. Liu, W. Chen, Z. Xu, Preparation and characterization of lamellar-like Mg(OH)₂ nanostructures via natural oxidation of Mg metal in formamide/water mixture, *Mater. Res. Bull.* 42 (2007) 1153–1158. doi:10.1016/j.materresbull.2006.09.008.
- [59] B. Downs, S. Robinson, H. Yang, P. Mooney, RRUFF Project, Dep. Geosci. Univ. Arizona. (2015). <http://rruff.info/>.
- [60] B. Humbert, M. Alnot, F. Quilès, Infrared and Raman spectroscopical studies of salicylic and salicylate derivatives in aqueous solution, *Spectrochim. Acta - Part A Mol. Biomol. Spectrosc.* 54 (1998) 465–476. doi:10.1016/S1386-1425(97)00239-4.
- [61] M.C. Alvarez-Ros, S. Sánchez-Cortés, J. V. García-Ramos, Vibrational study of the salicylate interaction with metallic ions and surfaces, *Spectrochim. Acta - Part A Mol. Biomol. Spectrosc.* 56 (2000) 2471–2477. doi:10.1016/S1386-1425(00)00328-0.
- [62] D. Philip, A. John, C.Y. Panicker, H.T. Varghese, FT-Raman, FT-IR and surface enhanced Raman scattering spectra of sodium salicylate, *Spectrochim. Acta - Part A Mol. Biomol. Spectrosc.* 57 (2001) 1561–1566. doi:10.1016/S1386-1425(01)00395-X.
- [63] M.A. Elbagerma, G. Azimi, H.G.M. Edwards, A.I. Alajtal, I.J. Scowen, In situ monitoring of pH titration by Raman spectroscopy, *Spectrochim. Acta - Part A Mol. Biomol. Spectrosc.* 75 (2010) 1403–1410. doi:10.1016/j.saa.2010.01.008.
- [64] P.J. Goulet, R.F. Aroca, Chemical adsorption of salicylate on silver - A systematic approach to the interpretation of surface-enhanced vibrational spectra, *Can. J. Chem.* 82 (2004) 987–997. doi:10.1139/v04-075.
- [65] L. Wasylina, E. Kucharska, Z. Weglinski, A. Puszko, *Chemistry of Heterocyclic Compounds, Vol.35, No. 2*, 1999, *Chem. Heterocycl. Compd.* 35 (1999) 210–218.
- [66] G. Świdorski, M. Kalinowska, I. Rusinek, M. Samsonowicz, Z. Rzączyńska, W. Lewandowski, Spectroscopic (IR, Raman) and thermogravimetric studies of 3d-metal cinchononates and dinicotinates, *J. Therm. Anal. Calorim.* 126 (2016) 1521–1532. doi:10.1007/s10973-016-5818-7.
- [67] M. Karabacak, S. Bilgili, A. Atac, Molecular structure investigation of neutral, dimer and anion forms of 3,4-pyridinedicarboxylic acid: A combined experimental and theoretical study, *Spectrochim. Acta - Part A Mol. Biomol. Spectrosc.* 135 (2015) 270–282. doi:10.1016/j.saa.2014.06.130.
- [68] Y. Song, X. Wang, S. Zhang, J. Wang, S. Gao, S. Chen, Lanthanide-Coordination Polymers with Pyridinedicarboxylic Acids: Syntheses, Structures, and Luminescent Properties, *Zeitschrift Für Anorg. Und Allg. Chemie.* 642 (2016) 681–691. doi:10.1002/zaac.201600135.
- [69] G. Lefèvre, T. Preočanin, J. Lützenkirchen, Attenuated total reflection - Infrared spectroscopy applied to the study of mineral - aqueous electrolyte solution interfaces: a general overview and a case study, in: T. Theophanides (Ed.), *Infrared Spectrosc.*, Intech, 2012. doi:10.5772/36459.

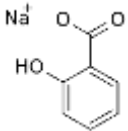
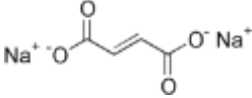
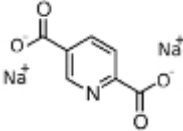
- [70] S.B. Johnson, T.H. Yoon, B.D. Kocar, G.E. Brown, Adsorption of organic matter at mineral/water interfaces. 2. Outer-sphere adsorption of maleate and implications for dissolution processes, *Langmuir*. 20 (2004) 4996–5006. doi:10.1021/la036288y.
- [71] M.M. Rakhimova, N.Z. Yusupov, T.M. Nurmatov, J.A. Davlatshoeva, L. Kvyatkovskaya, A.R. Bakhtibekova, M. Bobonazarov, Salicylate Coordination Compounds of Iron, Models of Their Formation, *Am. J. Chem.* 3 (2013) 23–29. doi:10.5923/j.chemistry.20130302.01.
- [72] M. Esmaily, J.E. Svensson, S. Fajardo, N. Birbilis, G.S. Frankel, S. Virtanen, R. Arrabal, S. Thomas, L.G. Johansson, Fundamentals and advances in magnesium alloy corrosion, *Prog. Mater. Sci.* 89 (2017) 92–193. doi:10.1016/j.pmatsci.2017.04.011.
- [73] Y. Yan, A. Maltseva, P. Zhou, X. Li, Z. Zeng, O. Gharbi, K. Ogle, M. Vaudescal, M. Lahaye, M. Esmaily, N. Birbilis, On the in-situ aqueous stability of an Mg-Li-(Al-Y-Zr) alloy: Role of Li, *Corros. Sci.* In Press (2019). doi:10.1016/j.corsci.2019.108342.
- [74] R.E. McNulty, J.D. Hanawalt, Some corrosion characteristics of high purity magnesium alloys, *J. Electrochem. Soc.* 81 (1942) 423–433. doi:10.1149/1.3071389.
- [75] S. Thomas, O. Gharbi, S.H. Salleh, P. Volovitch, K. Ogle, N. Birbilis, On the effect of Fe concentration on Mg dissolution and activation studied using atomic emission spectroelectrochemistry and scanning electrochemical microscopy, *Electrochim. Acta.* (2016). doi:10.1016/j.electacta.2016.05.164.
- [76] S.R. Ryu, I. Noda, Y.M. Jung, Positional Fluctuation of IR Absorption Peaks: Frequency Shift of a Single Band or Relative Intensity Changes of Overlapped Bands, *Am. Lab.* 43 (2011) 40–43.
- [77] S.R. Ryu, I. Noda, Y.M. Jung, What is the Origin of Positional Fluctuation of Spectral Features : True Frequency Shift or Relative Intensity Changes of Two Overlapped Bands?, *Appl. Spectrosc.* 64 (2010) 1017–1021. doi:10.1366/000370210792434396.
- [78] J.A. Dean, *Lange's Handbook of Chemistry*, 15th ed., McGraw-Hill, New York, 1999.
- [79] V. Masilamani, H.M. Ghaithan, M.J. Aljaafreh, A. Ahmed, R. Thagafi, S. Prasad, M.S. Alsalhi, Using a Spectrofluorometer for Resonance Raman Spectra of Organic Molecules, 2017 (2017). doi:10.1155/2017/4289830.
- [80] L. Pan, T. Frydel, M.B. Sander, X. Huang, J. Li, The Effect of pH on the Dimensionality of Coordination Polymers, *Inorg. Chem.* 40 (2001) 1271–1283. doi:10.1021/ic001012o.
- [81] M.C. Das, S.K. Ghosh, E.C. Sañudo, P.K. Bharadwaj, Coordination polymers with pyridine-2,4,6-tricarboxylic acid and alkaline-earth/lanthanide/transition metals: Synthesis and X-ray structures, *J. Chem. Soc. Dalton Trans.* (2009) 1644–1658. doi:10.1039/b814066a.
- [82] B. Ay, N. Dogan, E. Yildiz, I. Kani, A novel three dimensional samarium(III) coordination polymer with an unprecedented coordination mode of the 2,5-pyridinedicarboxylic acid ligand: Hydrothermal synthesis, crystal structure and luminescence property, *Polyhedron*. 88 (2015) 176–181. doi:10.1016/j.poly.2014.12.035.
- [83] S. Caglar, E. Dilek, S.H. Alisir, B. Caglar, New copper(II) complexes including pyridine-2,5-dicarboxylic acid: synthesis, spectroscopic, thermal properties, crystal structure and how these complexes interact with purified PON 1 enzyme, *J. Coord. Chem.* 69 (2016) 2482–2492. doi:10.1080/00958972.2016.1188295.
- [84] R.P. Eischens, W.A. Pliskin, The Infrared Spectra of Adsorbed Molecules, *Adv. Catal.* 10 (1958) 1–56. doi:10.1016/S0360-0564(08)60403-4.
- [85] F.P. Rotzinger, J.M. Kesselman-Truttman, S.J. Hug, V. Shklover, M. Grätzel, Structure and Vibrational Spectrum of Formate and Acetate Adsorbed from Aqueous Solution onto the TiO₂ Rutile (110) Surface, *J. Phys. Chem. B.* 108 (2004) 5004–5017. doi:10.1021/jp0360974.
- [86] J.D. Kubicki, L.M. Schroeter, M.J. Itoh, B.N. Nguyen, S.E. Apitz, Attenuated total reflectance Fourier-transform infrared spectroscopy of carboxylic acids adsorbed onto mineral surfaces, *Geochim. Cosmochim. Acta.* 63 (1999) 2709–2725. doi:10.1016/S0016-7037(99)00194-5.
- [87] K.D. Dobson, A.J. McQuillan, In situ infrared spectroscopic analysis of the adsorption of aromatic carboxylic acids to TiO₂, ZrO₂, Al₂O₃, and Ta₂O₅ from aqueous solutions, *Spectrochim. Acta - Part A Mol. Biomol. Spectrosc.* 56 (2000) 557–565. doi:10.1016/S1386-1425(99)00154-7.

Table 1. Chemical composition of pure Mg and alloys as analyzed by spark optical emission spectroscopy. The values are in ppm or in at. % when indicated.

	Mg (at.%)	Ag	Al	Ca	Ce	Cu	Fe	La	Mn	Ni	Pb	Si	Sn	Zn	Zr
CP-Mg342	99.96	<0.5	40	<1	7	4	342	<5	24	<2	<4	<1	<3	5	<5
HP-Mg 51	99.98	0.7	50	<1	<4	<1	51	<5	8	<2	<4	<1	<3	10	23

Journal Pre-proof

Table 2. Organic compounds studied in present work and respective inhibiting efficiency (IE) for CP-Mg342 and HP-Mg51. The tests were performed with Na salts at the initial pH of the electrolyte varying in the range from 5.3 to 6.7

Name	Abbreviation	Structural formula of neutralized acid	pK _a of respective acid	IE, % (CP-Mg342)	IE, % (HP-Mg51)
Sodium Salicylate	Sal		2.8*	84 ± 1	-244 ± 29
Sodium Fumarate	Fum		2.85* 4.10*	87 ± 1	58 ± 6
Sodium 2,5 – Pyridine-dicarboxylate	PDC		2.35** 4.64**	89 ± 1	74±5

the value given was measured at

* ionic strength of 0.1, and 25°C

** ionic strength of 0.5, and 20°C

Table 3. Synthetic reference samples used for the interpretation of Raman spectra.

Chemical composition	Preparation procedure
Mg(II)-Sal soluble complex	25 ml 0.1 M MgCl₂ (0.508 g MgCl ₂ ·6H ₂ O) + 0.05 M NaSal (0.200 g of salt)
Mg(OH) ₂	25 ml 0.1 M MgCl₂ (0.508 g MgCl ₂ ·6H ₂ O) + 25 ml 0.1 M NaOH (1.000 g NaOH). White precipitate was centrifuged and filtered
Mg(OH) ₂ in presence of Sal	25 ml 0.1 M MgCl₂ (0.508 g MgCl ₂ ·6H ₂ O) + 0.05 M NaSal (0.200 g of salt) + 25 ml 0.1 M NaOH (1.000 g NaOH) White precipitate was centrifuged and filtered.
Fe(OH) ₃	25 ml 0.1 M FeCl₃ (0.675g FeCl ₃ ·6H ₂ O) + 25 ml 0.1 M NaOH (1.000 g NaOH) Brown precipitate was centrifuged and filtered
Fe(III)-Sal soluble complex	25 ml 0.1 M FeCl₃ (0.675g FeCl ₃ ·6H ₂ O) + 0.05 M NaSal (0.200 g)
Fe(OH) ₃ in presence of Sal	25 ml 0.1 M FeCl₃ (0.675g FeCl ₃ ·6H ₂ O) + 0.05 M NaSal (0.200 g of salt) + 25 ml 0.1 M NaOH (1.000 g NaOH) Brown precipitate was centrifuged and filtered
Sal adsorbed on carbon steel	Carbon steel plate grinded with 800, 1200, 2400 SiC paper and immersed for 2 h in 25 ml solution of 0.05 M NaSal (0.200 g of salt, pH adjusted to 10.2 by 1M NaOH) and 0.1 M NaCl (0.146 g NaCl)

Table 4. IR and Raman spectral data (cm^{-1}) and band assignments for NaSal solution, CP-Mg342 exposed in NaSal solution, precipitated in presence of NaSal $\text{Mg}(\text{OH})_2$, soluble complex of Fe(III)Sal.

Sal Solution		CP-Mg342 surface + Sal		$\text{Mg}(\text{OH})_2$ + Sal		Fe(III)Sal		Assignment
IR	Raman	IR	Raman	IR	Raman	IR	Raman	
1624, 1592	1625, 1595	1605	1605	1603, 1589	1595, br	1602	1601	$\nu_{8b} + \nu(\text{C}=\text{O}) + \delta(\text{C}_\phi\text{-OH})$
1572	1574, br	1567, br	1575, br	1565, br	1575	1574		$\nu(\text{C-C})$ ring or $\nu_{\text{as}}(\text{COO}^-)$
-	-	1536, br	-	1531, br	-	1544		$\nu_{\text{as}}(\text{COO}^-)$
1489	1489	1470	1470, sh			1467	1468	C-C ring, (19a)
1457	1460	1449	1450	1447, s	1453, m	1455	1455	C-C ring or $\delta(\text{OH})$
1387	1387	1389, sh	1393, sh	1388	1392	1359	1350, s	$\nu_{\text{s}}(\text{COO}^-)$
1342	1347, br	1369, br	1375, s	1373, sh	1376, sh			$\nu_{\text{s}}(\text{COO}^-) + \delta \text{C}_{\text{ph}}\text{-O}$
1300, sh	1306	1309, br	1317, s		1317, s, br		1312, s	$\nu(\text{C-C})$ ring, 14
1254	1256	1250	1252	1254	1255	1242	1240, m	$\nu(\text{C}_\phi\text{-O})$
-	1225	-	-					δCH
1159	1160, vw	1157, vw	1160, vw				-	?
1147	1147	1140	1143, m			1146	1144	δCC (10)
1033	1034	1045, s	1044, s	1041	1043, br		1037, vw	δCH
861	867, w	877	-	872		887	886	
810	814, s	818	821		821		840	$\nu(\text{C}_\phi\text{-COO}^-) + (\text{C}_\phi\text{-OH}) + \delta_{\text{s}}(\text{COO}^-)$

ν - very; s -strong; m - medium, w - weak; sh - shoulder; br - broad.

ν indicates a stretching mode, δ an in-plane bending mode

(+) in-phase movement; (-) out-of-phase movement;

C_ϕ - carbon of the aromatic ring

Table 5. IR spectral data (wavenumbers, cm^{-1}) and band assignments for NaPDC solution, CP-Mg342 exposed in NaPDC solution.

NaPDC Solution	CP-Mg342 surface + PDC	Assignment
-	1724	$\nu\text{C=O}$
1652	1607	$\nu_{\text{as}}(\text{COO}^-)$
1581, br	1589	$\nu_{\text{as}}(\text{COO}^-)$; $\nu\text{CC ring} + \nu\text{CN} + \delta\text{CCH} + \delta\text{CNH}$
1480	1480, sh	$\nu(\text{CN}) + \delta\text{CCH} + \nu(\text{C-O})$
	1457, sh	$\nu_{\text{s}}(\text{COO}^-)$
1385, vs	1385, vs	$\nu_{\text{s}}(\text{COO}^-)$
1362	1362	$\nu_{\text{s}}(\text{COO}^-)$
1278	1286	$\nu\text{C-O} + \nu\text{CC ring} + \nu\text{CN}$
1178	1178	$\delta(\text{CC}) + \nu(\text{CC}) + \delta(\text{CH})$
1121	1121	
1030	1036	$\nu\text{CC ring} + \nu\text{CN} + \delta\text{CCH}$
826	826, vw	$\delta_{\text{s}}(\text{COO}^-)$

ν - very; s -strong; m - medium, w - weak; sh - shoulder; br - broad.

ν indicates a stretching mode, δ an in-plane bending mode

(+) in-phase movement; (-) out-of-phase movement;

C_{ϕ} – carbon of the aromatic ring

Table 6. IR spectral data (wavenumbers, cm^{-1}) and band assignments for 0.05 M NaFum solution and CP-Mg342 exposed in the same solution during 2 h.

NaFum Solution	CP-Mg342 surface + Fum	Assignment
1560	1569	$\nu_{\text{as}}(\text{COO}^-)$
1374	1372 1395 (sh)	$\nu_{\text{s}}(\text{COO}^-)$
1213	1213	δCH
980	988	δCH

Journal Pre-proof

Fig. 1. Optical images (a-e) and hydrogen evolution (g) of CP-Mg342 and HP-Mg51 samples being in contact with 0.1 M NaCl solution (a,b) and in 0.1 M NaCl solution with addition of 0.05 M inhibitors: sodium salicylate (c, d), 2,5-pyridin-dicarboxylate (e) and fumarate (f). Left part of each figure corresponds to the dry sample removed from the flow cell after 2h of experiment. Right part of each figure (higher magnification) illustrates the *in situ* surface appearance during exposure.

Fig. 2. SEM micrographs of CP-Mg342 surface after 30 minutes contact with flowing 0.1 M NaCl solution (a) and 0.1 M NaCl solution with addition of 0.05 M inhibitors: sodium salicylate (b), 2,5-pyridin-dicarboxylate (c) and fumarate (d).

Fig. 3. (a) Fragments of *in situ* Raman spectra recorded on CP-Mg342 in 0.1M NaCl in absence and in presence of corrosion inhibitors; (b) growth kinetics of $Mg(OH)_2$ recorded on CP-Mg342 in 0.1M NaCl with or without the corrosion inhibitors, mean value and standard deviation through the map.

Fig. 4. (a) *In situ* Raman spectra of CP-Mg342 and HP-Mg51 after 2 h of exposure in 0.1 M NaCl + 0.05 M NaSal solution. These spectra were compared with the following reference spectra: saturated solution of pure NaSal, $Mg(OH)_2$ precipitated in presence of NaSal, Fe(III)Sal complex. (b) IR spectrum of CP-Mg342 just after 2 h of exposure in 0.1 M NaCl + 0.05 M NaSal solution compared with following reference spectra: 0.05 M solution of pure NaSal, $Mg(OH)_2$ precipitated in presence of NaSal, Fe(III)Sal complex.

Fig. 5. (a) *In situ* Raman spectrum recorded after exposure of CP-Mg342 in 0.1 M NaCl + 0.05 M NaPDC solution for 20 min compared with the spectrum saturated solution solution of pure NaPDC; (b) IR spectrum of CP-Mg342 just after 2 h of exposure in 0.1 M NaCl + 0.05 M NaPDC solution compared with spectrum of 0.05 M solution of pure NaPDC.

Fig. 6. (a) *In situ* Raman spectrum of CP-Mg342 after 40 min of exposure in 0.1 M NaCl + 0.05 M NaFum solution compared with the spectrum of saturated solution solution of pure NaFum; (b) IR spectrum of CP-Mg342 just after 2 h of exposure in 0.1 M NaCl + 0.05 M NaFum solution compared with spectrum of 0.05 M NaFum solution.

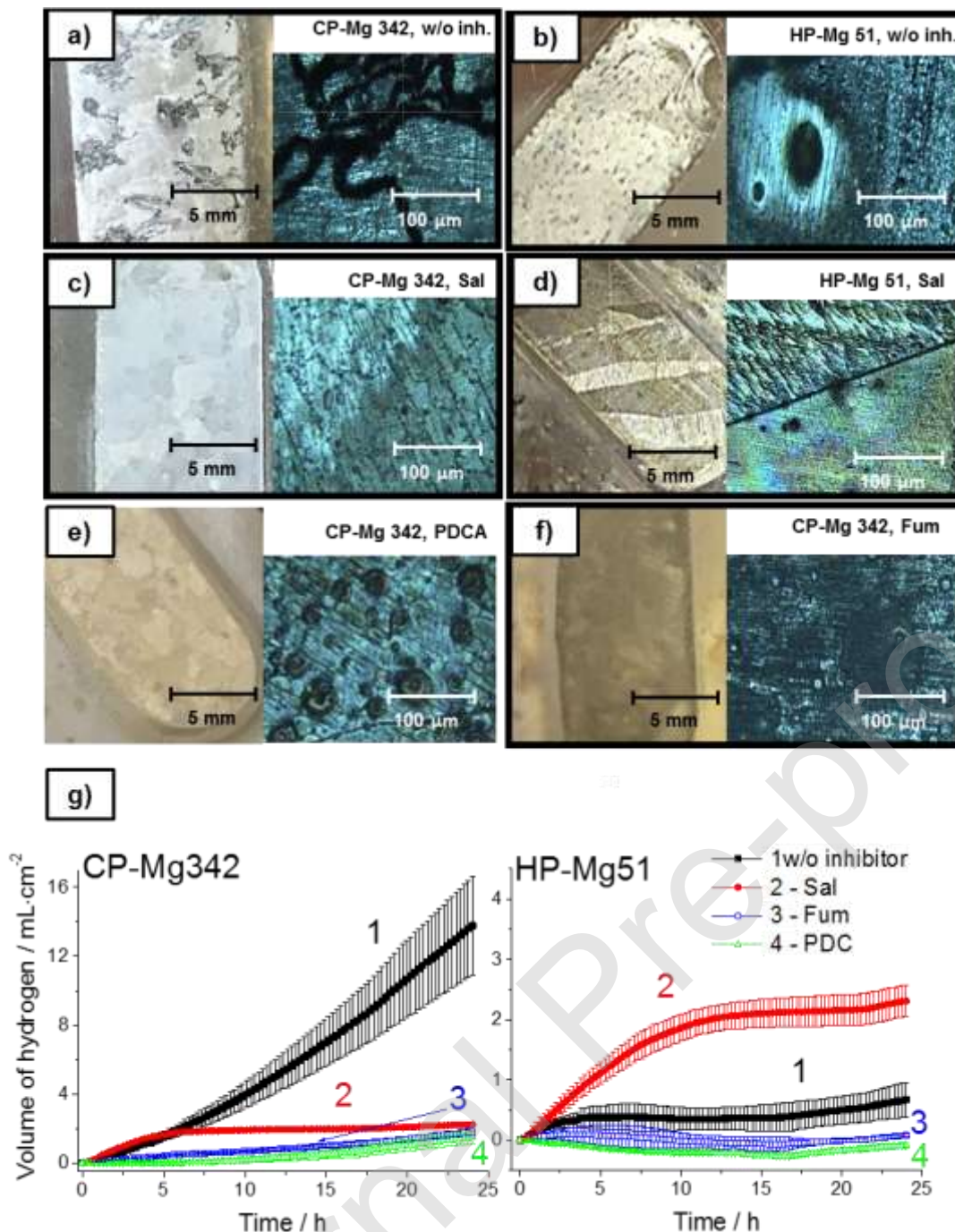
Fig. 7. Qualitative depth profiles of CP-Mg342 after 30 min of exposure in 0.1 M NaCl solution in absence of inhibitors and after 2 h of exposure in presence of NaSal (b), PDC (c), Fum (d). Dashed line shows the interface between the oxide layer and metal bulk.

Fig. 8. Schematic representation of Sal inhibition mechanism: 1-initial stage, 2-dissolution of Fe-rich inclusions and stabilization of $Mg(OH)_2$ nano-crystals. The formed film prevents Cl adsorption.

Fig. 9. Schematic representation of PDC inhibition mechanism via precipitation of PDC-coordination polymer. The formed film prevents Cl accumulation.

Fig. 10. Schematic representation of Fum inhibition mechanism via adsorption of carboxylate limiting Cl access to the surface.

Journal Pre-proof

**Fig. 1.**

Optical images (a-e) and hydrogen evolution (g) of CP-Mg342 and HP-Mg51 samples being in contact with 0.1 M NaCl solution (a,b) and in 0.1 M NaCl solution with addition of 0.05 M inhibitors: sodium salicylate (c, d), 2,5-pyridin-dicarboxylate (e) and fumarate (f). Left part of each figure corresponds to the dry sample removed from the flow cell after 2h of experiment. Right part of each figure (higher magnification) illustrates the *in situ* surface appearance during exposure.

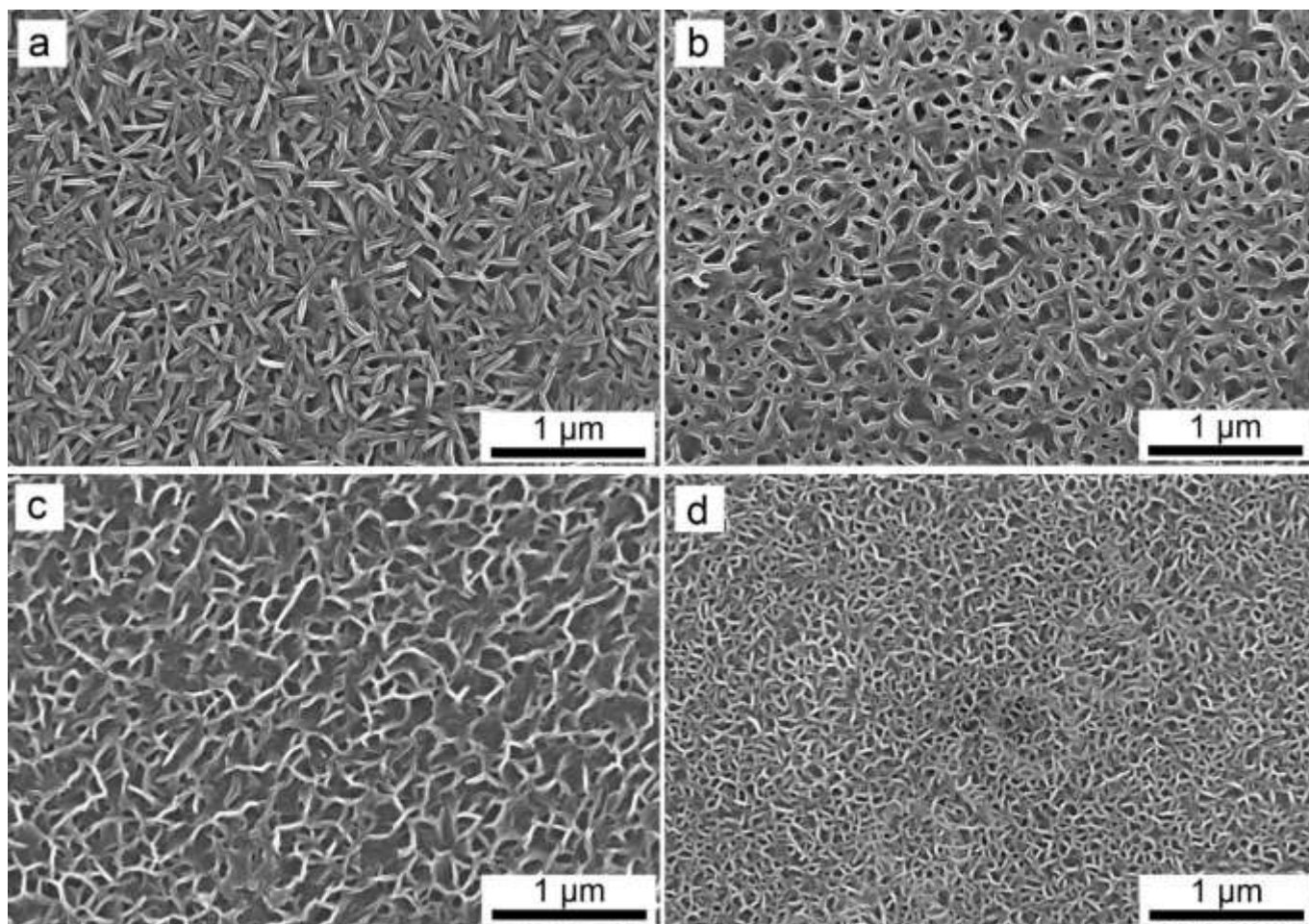


Fig. 2.

SEM micrographs of CP-Mg342 surface after 30 minutes contact with flowing 0.1 M NaCl solution (a) and 0.1 M NaCl solution with addition of 0.05 M inhibitors: sodium salicylate (b), 2.5-pyridin-dicarboxylate (c) and fumarate (d).

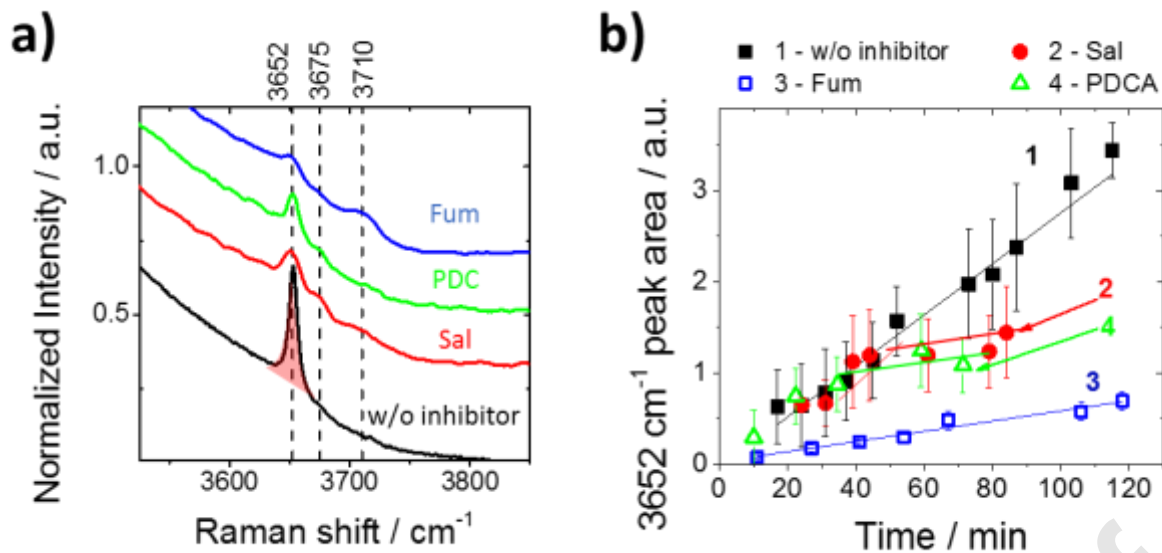


Fig. 3. (a) Fragments of *in situ* Raman spectra recorded on CP-Mg342 in 0.1M NaCl in absence and in presence of corrosion inhibitors; (b) growth kinetics of $\text{Mg}(\text{OH})_2$ recorded on CP-Mg342 in 0.1M NaCl with or without the corrosion inhibitors, mean value and standard deviation through the map.

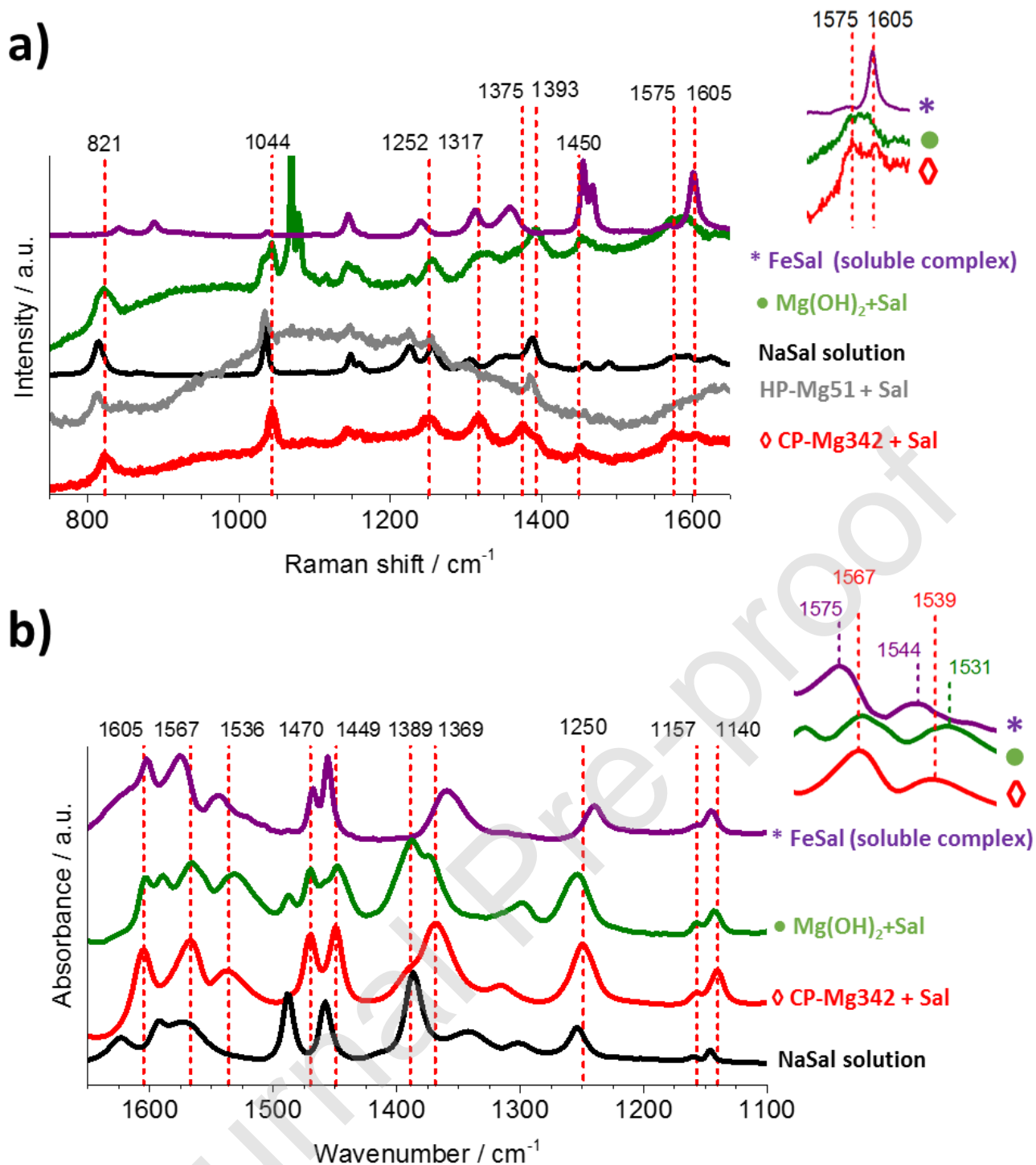


Fig. 4. (a) *In situ* Raman spectra of CP-Mg342 and HP-Mg51 after 2 h of exposure in 0.1 M NaCl + 0.05 M NaSal solution. These spectra were compared with the following reference spectra: saturated solution of pure NaSal, Mg(OH)₂ precipitated in presence of NaSal, Fe(III)Sal complex. (b) IR spectrum of CP-Mg342 just after 2 h of exposure in 0.1 M NaCl + 0.05 M NaSal solution compared with following reference spectra: 0.05 M solution of pure NaSal, Mg(OH)₂ precipitated in presence of NaSal, Fe(III)Sal complex.

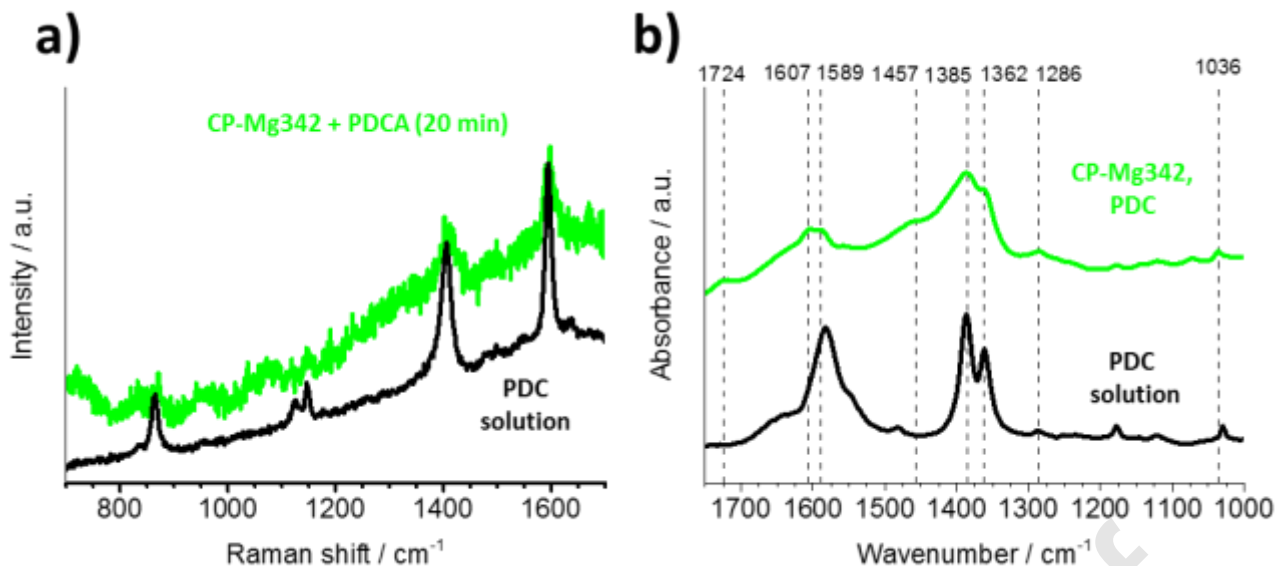


Fig. 5. (a) *In situ* Raman spectrum recorded after exposure of CP-Mg342 in 0.1 M NaCl + 0.05 M NaPDC solution for 20 min compared with the spectrum saturated solution solution of pure NaPDC; (b) IR spectrum of CP-Mg342 just after 2 h of exposure in 0.1 M NaCl + 0.05 M NaPDC solution compared with spectrum of 0.05 M solution of pure NaPDC.

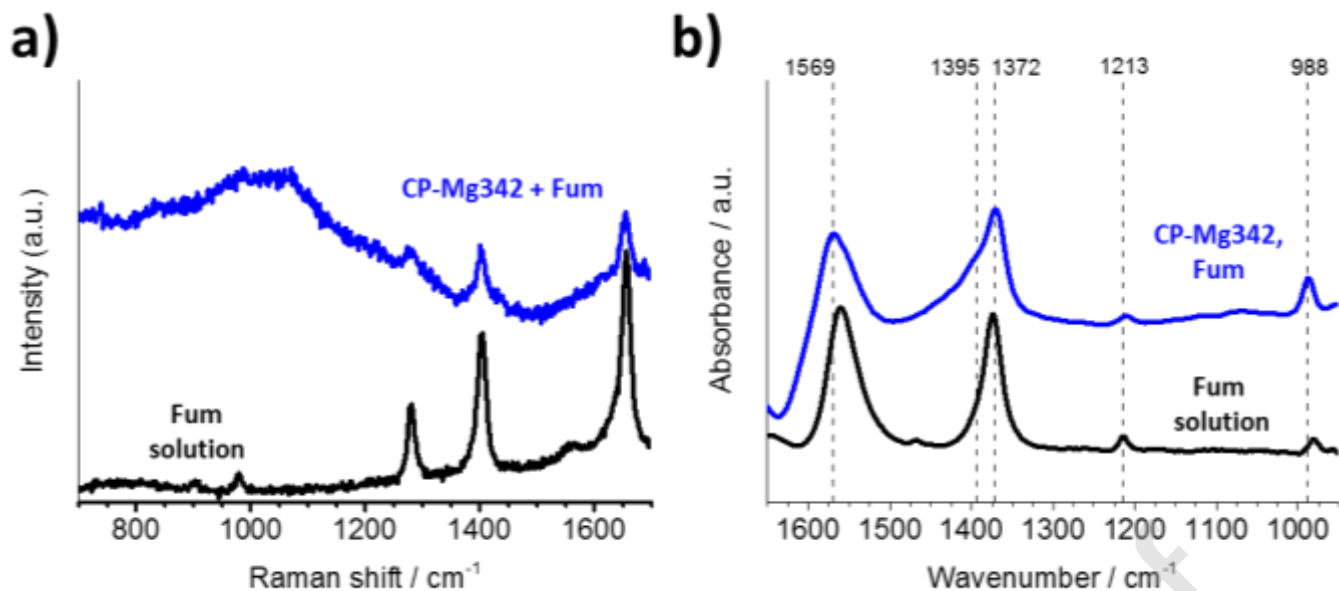


Fig. 6. (a) *In situ* Raman spectrum of CP-Mg342 after 40 min of exposure in 0.1 M NaCl + 0.05 M NaFum solution compared with the spectrum of saturated solution solution of pure NaFum; (b) IR spectrum of CP-Mg342 just after 2 h of exposure in 0.1 M NaCl + 0.05 M NaFum solution compared with spectrum of 0.05 M NaFum solution.

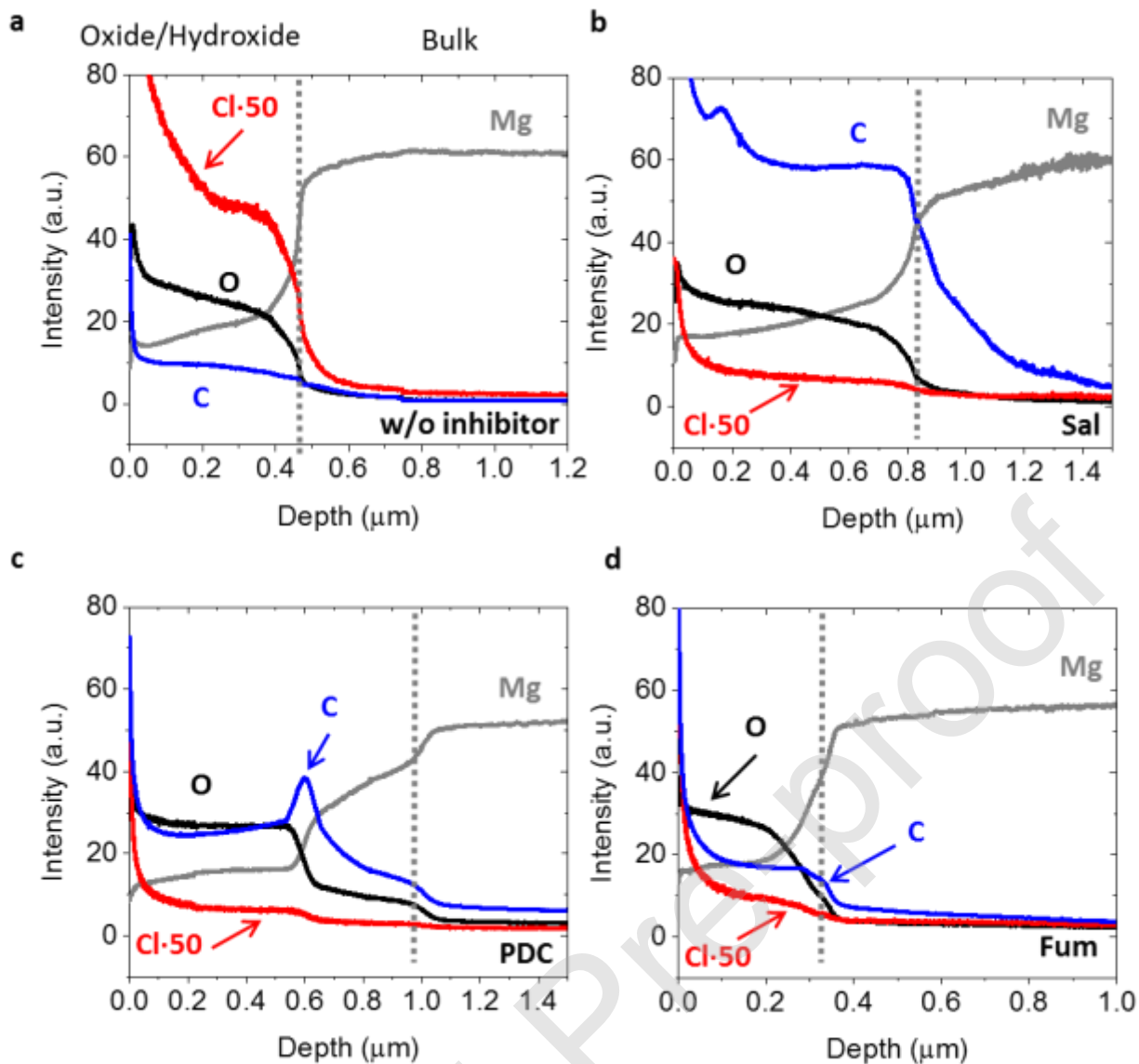


Fig. 7. Qualitative depth profiles of CP-Mg342 after 30 min of exposure in 0.1 M NaCl solution in absence of inhibitors and after 2 h of exposure in presence of NaSal (b), PDC (c), Fum (d). Dashed line shows the interface between the oxide layer and metal bulk.

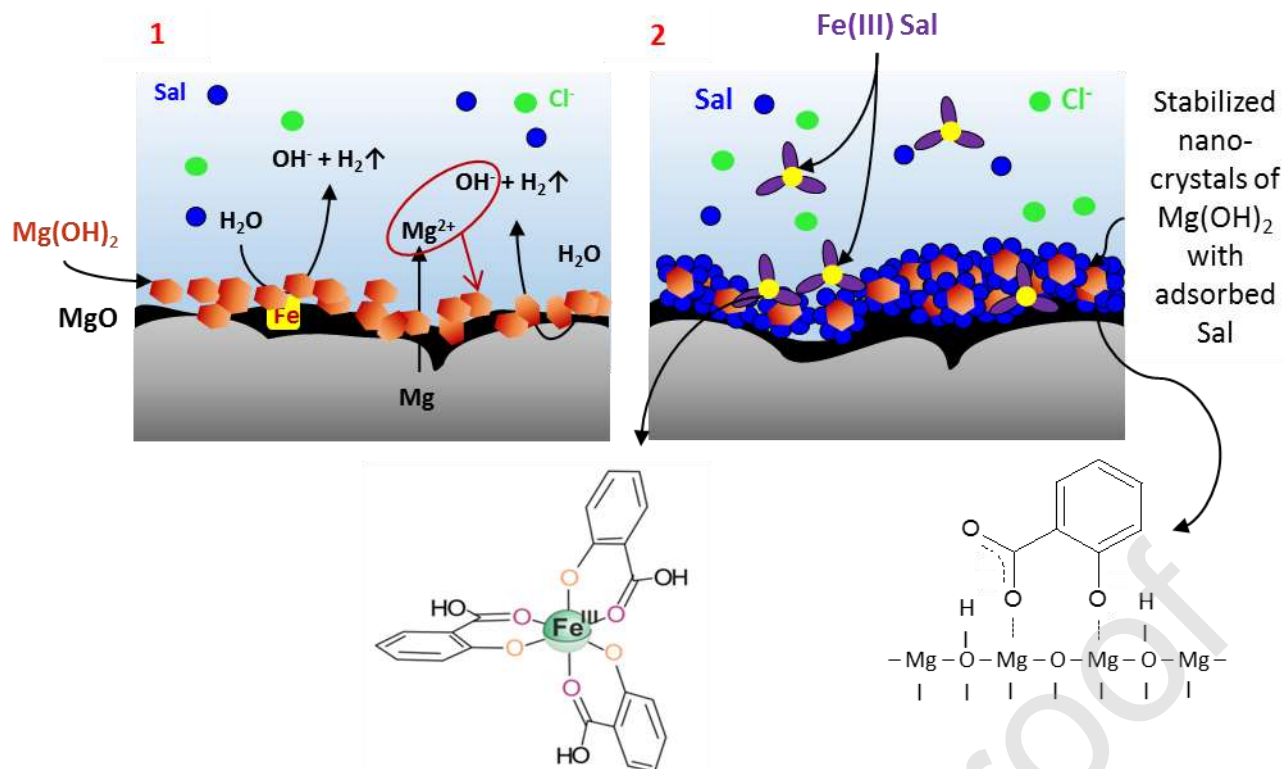


Fig. 8. Schematic representation of Sal inhibition mechanism: 1-initial state, 2-dissolution of Fe-rich inclusions and stabilization of $\text{Mg}(\text{OH})_2$ nano-crystals. The formed film prevents Cl adsorption.

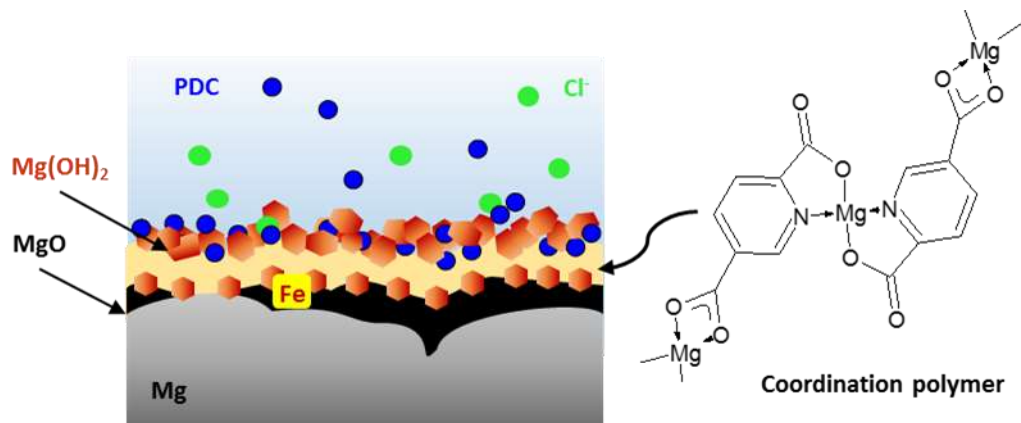


Fig. 9. Schematic representation of PDC inhibition mechanism via precipitation of PDC-coordination polymer. The formed film prevents Cl accumulation.

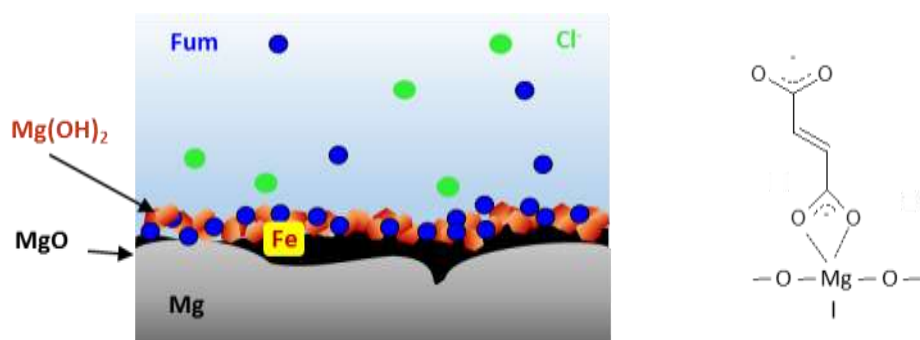


Fig. 10. Schematic representation of Fum inhibition mechanism via adsorption of carboxylate limiting Cl access to the surface.